POLITECNICO DI TORINO

Master's Degree in Biomedical Engineering

Master's Degree Thesis

Development of a Bluetooth device for Pulse Wave Velocity estimation using load cells

Supervisors

Prof. Danilo DEMARCHI

Ph.D Alessandro SANGINARIO

Ph.D Irene BURAIOLI

Candidate

Pierluigi NATALE

December 2022

Abstract

With 17.9 million deaths per year, approximately 32% of all annual deaths, cardiovascular disease (CVD) is the world's largest cause of death. Early detection and treatment of CVD can significantly lower the risk of premature death and ensure that patients lead normal lives. Among the several predictive factors, arterial stiffness has been found to be a useful indicator of cardiovascular risk and has a close relationship with Pulse Wave Velocity (PWV). Pulse Wave Velocity (PWV), which is often measured between the carotid and femoral sites, measures the speed of propagation of the pressure wave inside the arteries.

For this reason, this thesis aims to develop a low-cost, non-invasive Bluetooth device for PWV estimation. The sensitive elements used are digital micro force load cells produced by Honeywell, which behave like force sensors: placed on the skin in proximity of an artery, they can detect the smallest force variations caused by the artery pulse wave. These sensors are also chosen for their dimensions to find an alternative to tonometers used in the probes of ATHOS, an experimental device developed by the MiNES research group in Politecnico di Torino where this work has been conducted.

Firstly, an analysis of the state of the art about load cells and force sensors on the market was carried out. After choosing the sensor, the focus was shifted to implementing a read-out firmware to extract data collected by the sensor and, secondly, its characterization.

After implementing the Bluetooth Low Energy data transmission among sensors and the laptop, the sensors have been integrated within a modified version of the ATHOS probe holder. For the real-time visualization of the pulse wave signal, a Graphic User Interface of the experimental system has been adjusted to the sensor in use.

Finally, the final system was tested in "Ospedale Città della Scienza e della Salute" in Turin, where the clinical tests were carried out, followed by data processing and statistical analysis.

Acknowledgements

Table of Contents

List of Tables

List of Figures

Acronyms

CVD
: Cardiovascular Disease

MEMS
: Micro-Electro-Mechanical System

GPIO
: General Purpose Input/Output

ADC
: Analog to Digital Converter

BLE
: Bluetooth Low Energy

CS
: Chip Select

GND
: Ground

GUI
: Graphic User Interface

HW
: Hardware

MISO
: Master-In Slave-Out

MOSI
: Master-Out Slave-In

PWV
: Pulse Wave Velocity

SCLK
: SPI Clock

SPI
: Serial Peripheral Interface

SW
: Software

UART
: Universal Asynchronous Receiver-Transmitter

PTT
: Pulse Transit Time

PWD
: Pulse Wave DIstance

Chapter 1

Introduction

Cardiovascular diseases (CVDs) consist of a group of disorders related to the heart and blood vessels, like coronary heart, peripheral heart, cerebrovascular and rheumatic diseases, that can lead an individual to have heart attacks, strokes or ischemia. According to the World Health Organization [1], CVDs are the main cause of mortality worldwide. The number of deaths due to these groups of diseases has grown over the years, from 1990 with 12.1 million deaths to 2019 with 17.9 million deaths [2] which number represents 32 % of the global deaths in that year.

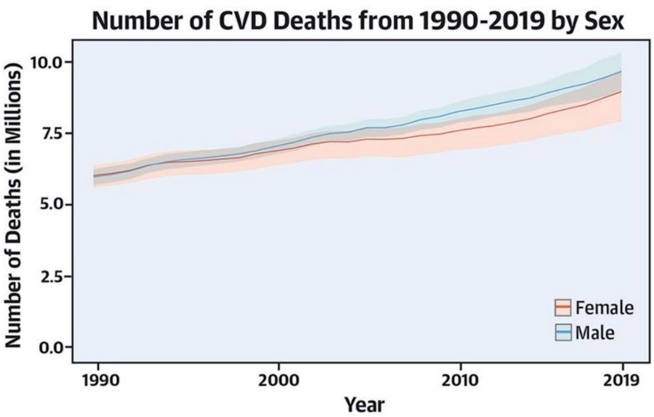

Figure 1.1: Number of CVD deaths over time by sex [2].

These numbers are likely to increase in the next years due to ageing and population growth worldwide; such an amount of subjects consequently goes to the burden of total health care costs. In fact, in parallel with the growth in the number of deaths, the costs associated with CVDs have also increased in recent years, as per the report prepared by the Centre for Economic and Business Research in 2014 [3]. These costs include not only the expense of hospitalization and patient care (direct costs) but also the so-called indirect costs which comprise mortality costs (lost earnings due to CVDs-related premature deaths) and morbidity costs (lost earnings due to lost productivity, including lost employment of currently employed individuals and sickness).

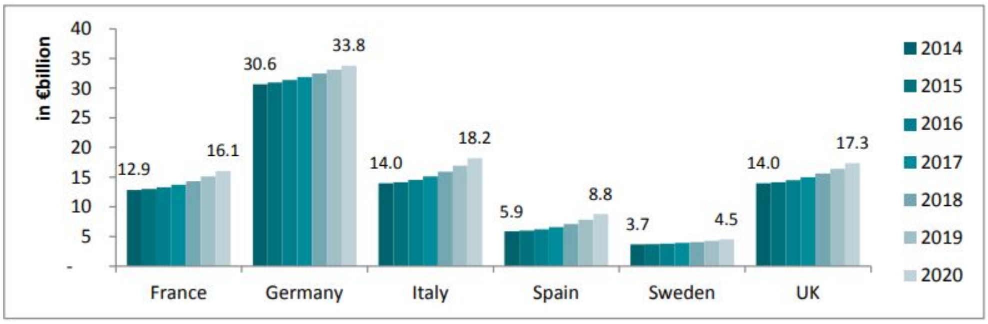

Figure 1.2: Healthcare cost of CVD, forecasts 2014-2020, in €billion [3]. (Source: Cebr analysis)

Relying on these data, earlier detection and treatment of cardiovascular diseases is extremely important. For that reason, research focuses on the improvement of existing diagnostic systems and discovering more effective ones.

To assess cardiovascular risk, there are many predictive parameters, among which one of the most substantial and valid is arterial stiffness. Its effectiveness has been proven over the past years; moreover, it's significantly correlated to the Pulse Wave Velocity, i.e. the propagation speed of the pulse wave inside arteries, through direct proportionality. For PWV estimation, most non-invasive devices used in clinic applications are based on applanation tonometry, by acquiring signals from two different points on the body (typically from the carotid and femoral artery). These devices, which we will discuss in Chapter 2 more in detail, are non-invasive, but they have high costs and low portability.

To overcome these problems, the MiNES Research Group (Micro&Nano Electronic Systems) in Politecnico di Torino developed the ATHOS system [4] [5]: two MEMS pressure sensors are used as tonometers and encapsulated in two pen-shaped supports. These sensors used are the LPS22HB [6] provided by STMicroelectronics but nowadays they are prototypical and still not patented yet. For that reason, this thesis aims to find a sensor that will replace the tonometer while maintaining its low costs and small dimensions to keep the system unchanged.

In the first part of the thesis, a general introduction to the physiology of the cardiovascular system is provided, followed by a description of PWV, the devices used in clinics to measure it, the sensor chosen for the thesis project and an overview of all hardware and software used during the thesis.

After that, the firmware implementation for the correct sensor readout is described, which is followed by its characterization and the setup for doing it. In the subsequent chapter, the integration with the ATHOS Bluetooth Low Energy (BLE) system is performed, with a general discussion about its main components and changes made to the system, with an explication of the firmware used in this phase.

In the end, data acquisition is performed on several patients in “Ospedale Città della Scienza e della Salute” in Turin where the system developed in this thesis is compared with SphygmoCor, the gold standard of the PWV evaluation. After tests have been performed, data acquired are subject to post-processing and statistical analysis.

Figure 1.3: View of the thesis' system: in the foreground, the probes in the base station are shown. They are connected via USB to the laptop, where the GUI is shown.

Chapter 2

Background

This section carried out a general overview of cardiovascular physiology, followed by a description of the arterial pulse. After a mention of the concept of PWV and its utility, the devices currently used in the market to detect it are shown. Finally, there is a description of all the devices and software used during the thesis period.

2.1 Cardiovascular physiology

The cardiovascular system, also defined as the vascular or circulatory system, is constituted by the heart, the lymphatic system, blood and a network of blood vessels through which the heart pumps blood all over the human body [7]. The main function of the cardiovascular system is the exchange of materials between capillaries and cells: specifically, cells extracted from the bloodstream nutrients, hormones, electrolytes, oxygen (O_2) and other substances and excreting waste products and carbon dioxide (CO_2) are taken away by blood. The mechanism just described is known as *systemic circulation*. There is another type of circulation, the *pulmonary circulation*, involving the blood circulation between the lungs and heart: in pulmonary alveoli, the blood absorbs oxygen (O_2) and releases carbon dioxide (CO_2) that is expelled with exhalation [8].

As said a few lines up, the cardiovascular system is composed of three principal components:

- ***Heart***: striate muscle that pumps blood inside blood vessels;

- ***Blood***: an organic, red-coloured liquid that circulates in the cardiovascular system distributing to all districts of the body and performing fundamental metabolic functions;

- ***Blood Vessels***: through them, the blood can flow along the whole human body. Based on their diameter and functionality, they can be divided into arteries, veins and capillaries.

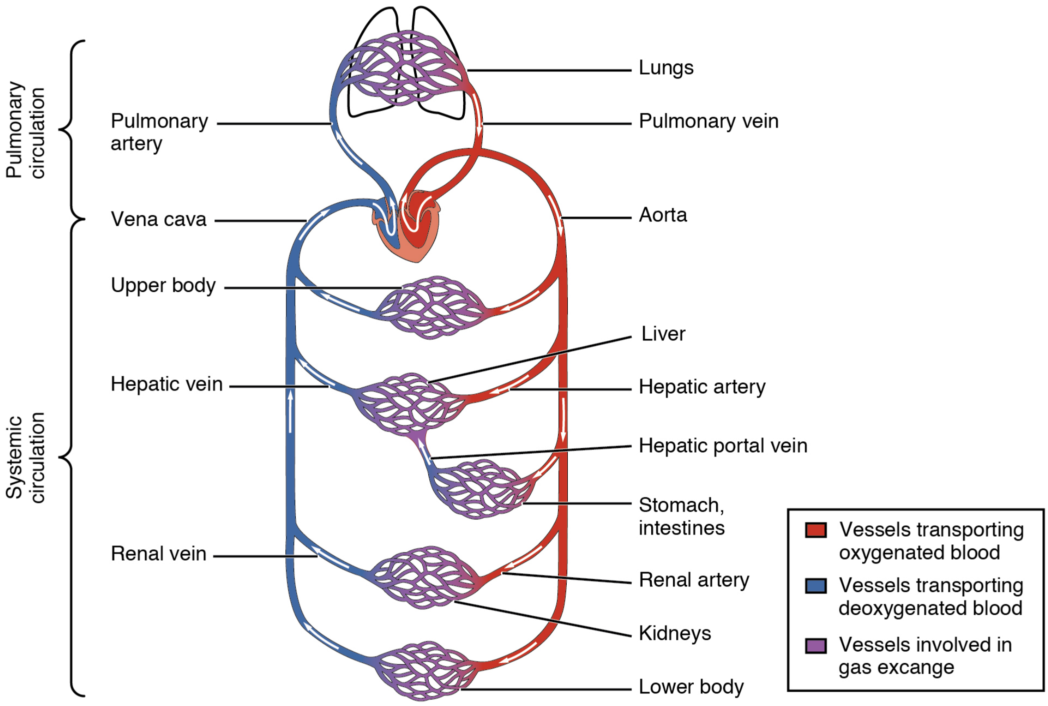

Figure 2.1: Schematic view of cardiovascular circulation [9].

2.1.1 Heart

The heart is a striated muscle that generates the necessary force to pump blood inside blood vessels. It is located within the rib cage, between the lungs in a space called *mediastinium*, and it has the size of a closed fist and a weight of about 200-300 grams. It consists of two sides and four heart chambers: right atria and ventricle, and left atria and ventricle. The right and the left side perform different functions: while the right side manages the pulmonary circulation oxygenating blood in exchange for secreting carbon dioxide, the left one deals with the systemic circulation [10].

An external membrane called *pericardium* surrounds the heart, protecting it from nearby mediastinal structures. Three layers make it up: the outermost is the fibrous pericardium, a tough, dense connective layer whose function is to protect the heart fixed in the thorax and prevent its overstretching. Further inland is the fibrous pericardium, which is composed of the parietal pericardium, a thin layer fused with the fibrous pericardium, and the visceral pericardium (also known as *epicardium*) that is firmly attached to the heart's surface. These two layers are separated by the pericardial fluid, contained in the pericardial cavity, which is essential to decrease friction during heart contraction and relaxation.

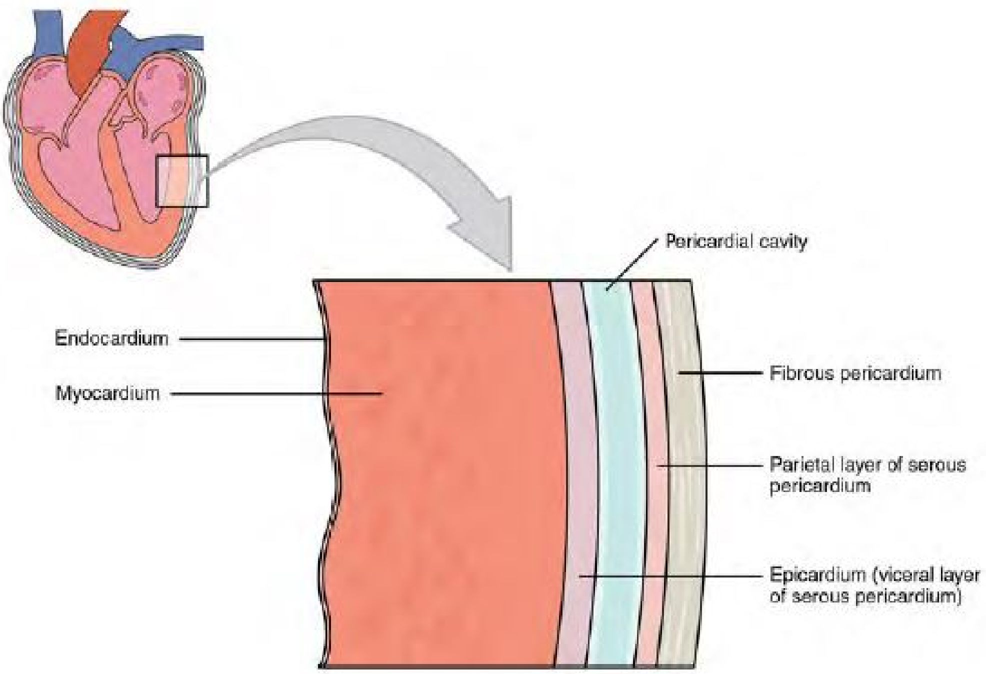

Figure 2.2: Zoom of the the heart's membranes [9].

Below these membranes lies the *myocardium*, the cardiac muscle that makes up the four cardiac chambers: right atria and ventricle, which perform the pulmonary circulation, and left atria and ventricle, which perform the systemic circulation. Atria are divided by the interatrial septum and the ventricle by the interventricular septum to keep oxygenated and deoxygenated blood apart. Moreover, atrioventricular septa divide the atria from the ventricles [7]. The correct direction of the blood flow through the heart is maintained by four heart valves: in particular, the two atrioventricular valves (mitral valve on the left side and tricuspid valve on the right side) prevent blood reflux in the atrium when the ventricle is contracting, while the two semilunar valves, located between the ventricles and the major arteries, prevent blood reflux from arteries to ventricle when ventricles relax.

All heart chambers are lined with *endocardium*, an epithelium layer that surrounds also the heart's valves and proceeds into vessels.

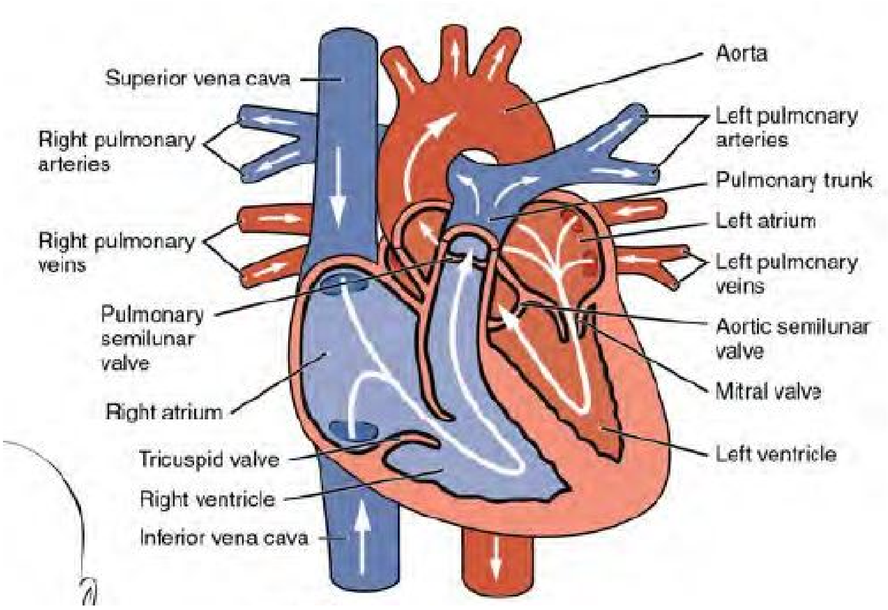

Figure 2.3: Heart anatomy [9].

Cardiac Cycle

The cardiac cycle can be defined as the set of events associated with blood flow through the heart during a single beat [8]. It can be divided summarily into two main stages: *systole* is the period of contraction of a chamber while *diastole* is the period of relaxation.

More specifically, the cardiac cycle starts with the contraction of the atria, moves through ventricular systole, atrial diastole, and ends with ventricular diastole before starting again. The flux of blood through heart chambers is driven by the difference in pressure: indeed, when atria are in diastole, the blood flows from veins into the atria (the so-called venous return) because the pressure in veins is higher than in the atria. The pressure in the two atria is raised by an increase in blood volume within them. The atrioventricular valve passively opens and allows blood to flow into the ventricle when the pressure outside the ventricle exceeds that inside. The semilunar valve is now closed to prevent blood from flowing backwards from the artery (which is under high pressure) to the ventricle (at low pressure). While the ventricle is still relaxed (in diastole), atrial contraction (atrial systole) forces blood into it to completely fill it and raise the pressure inside the chamber. The atrioventricular valve closes as a result of the ventricle's high pressure. Then, atrial diastole (atrial relaxation) and ventricular systole (ventricular contraction) take place concurrently [10]. In particular, as the ventricle contracts, the pulmonary artery and aorta experience a sudden rise in pressure that is greater than diastolic pressure. Due to the pressure gradient, the semilunar valve opens, and the right and left ventricles flow blood into the pulmonary trunk and aorta, respectively. After ventricular ejection, ventricular diastole takes place, and when ventricular pressure drops below that of the artery, semilunar valves close.

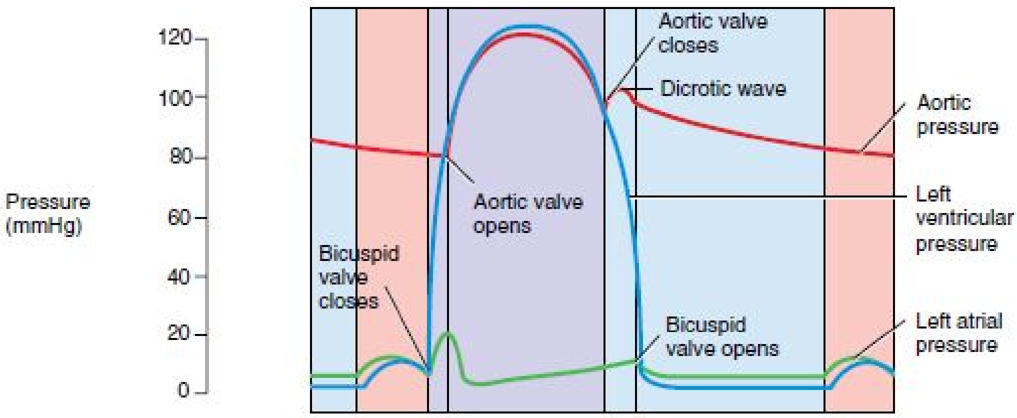

Figure 2.4: The cardiac cycle [11].

Heart's electrical activity

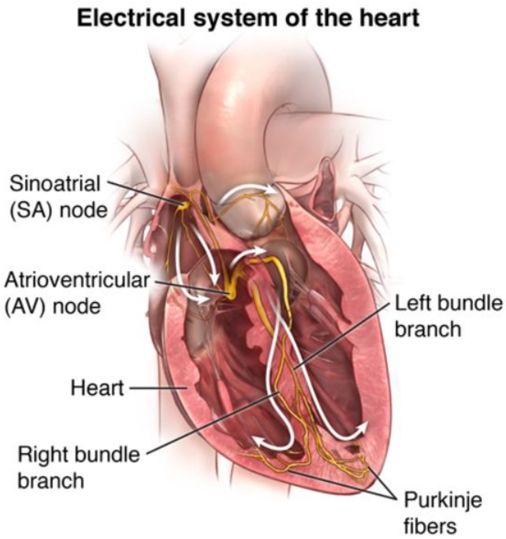

Figure 2.5: Electrical system of the heart [12].

An electrical conduction system directs the contraction of the atria and ventricles to ensure the proper heart-pumping function.

In reality, the sinoatrial node (SA node), which is situated in the upper section of the right atrium, produces the stimulus rather than the heart receiving any electrical impulses from the central nervous system. Under typical circumstances, the SA node regularly produces an electrical stimulus, 60 to 100 times per minute, which swiftly spreads to the entire atria. The atrioventricular node (AV node), located in the interatrial septum, receives the electrical signal through the internodal route, which simultaneously depolarizes the cardiac cells of the atria. The atrioventricular septum, which separates the atria from the ventricles and cannot be depolarized, leaves the AV node as the only route to the ventricles [7].

Additionally, the AV node introduces a delay of around 100 ms since it propagates electrical impulses more slowly than the SA node. From here, the conduction channel continues downward via the Purkinje fibres at the heart's apex and the bundle of His, which is located in the interventricular septum. To pump blood into the arteries, depolarization spreads from the apex to the upper section of the ventricles in this manner.

2.1.2 Blood

Blood performs many functions in the body, including providing nutrients and oxygen to the tissues as well as eliminating waste and carbon dioxide. Blood also aids in regulating body temperature by uniformly dispersing the heat generated by cellular chemical activity throughout the body. Additionally, it contributes to maintaining homeostasis and keeps the pH constant by the excretion or reabsorption of hydrogen and bicarbonate ions. Additionally, the blood supports the body's defence against the invasion of germs and their toxins since it contains antibodies and antitoxins, as well as neutrophil and monocyte phagocyte activity.

It is made up of cells and cell fragments suspended in a complicated extracellular matrix. The extracellular matrix of blood is remarkable in that it is a fluid, making it a connective tissue. Its composition always changes as it travels through the capillaries as a result of interactions with the interstitial fluid. Despite this, the majority of the constituents are still there.

It is made up of two distinct parts that can be separated by centrifugation: a liquid phase, the plasma, and a solid phase made up of cells and cell-derived materials, also known as figurative elements. About 54-58% of blood is made up of plasma which contains proteins, carbohydrates, fats, and minerals. Its primary function is to permit the movement of various substances, including nutrients, hormones, proteins, and products of cell metabolism, as well as to support the immune system by carrying antibodies that combat infections. In men and women, the metaphorical blood volume is roughly 46% and 42%, respectively [13]. The three main components of the blood are *red blood cells*, *white blood cells* and *platelets*.

Red blood cells, also called erythrocytes, regulate gaseous exchange in the body's organs and tissues by supplying oxygen and removing carbon dioxide. The supply of oxygen is provided by haemoglobin, a molecule that contains four atoms of iron each able to bond to one molecule of oxygen. They have the unique shape of a biconcave disc which ought to enable the cell to diffuse oxygen more quickly. Additionally, this form provides a sizable surface area in relation to cell volume, allowing the red blood cell to squirm into tiny arteries without substantially altering the membrane's form in a way that could harm it [11].

White blood cells, also called leukocytes, are a crucial component of the immune system and play a crucial role in the body's defence. They are in charge of eliminating infectious pathogens and secreting things like antibodies. To go to the various body sections, they employ the circulatory system.

Platelets, also called thrombocytes, are small, cell-free shards created in the bone marrow and discharged into the bloodstream. They participate in the blood clotting process, enabling quick treatment of wounds and traumas. In fact, they stick to the site and gather into clots that block the wound. They also exude chemicals that attract coagulation factors and encourage the aggregation of additional platelets.

Blood Pressure

Blood pressure is defined as the force that the blood exerts against the walls of blood vessels or the heart's chambers [7]. Typically it's expressed in mmHg (millimetres of mercury) and it's produced by the ventricles pumping. Systolic and diastolic blood pressure readings result in two numbers, 110/70 mmHg for example. Systolic pressure, the higher of the two pressures, is a measure of blood pressure when the left ventricle is contracting. Instead, diastolic pressure, the lower number, is a measure of blood pressure when the left ventricle is relaxed and not contracting.

Blood pressure is affected by several factors, like cardiac output (blood pumped out from the heart in one minute), circulating volume, peripheral resistance (provided by blood vessels), and blood viscosity, but there are also some hormones that regulate it, i.e. baroreceptors, chemoreceptors, etc.

Blood pressure drops when the blood moves further from the heart. Most frequently, blood pressure is measured in the brachial artery, where the typical systolic and diastolic ranges are 90 to 120 mmHg and 60 to 80 mmHg, respectively [14]. Systemic blood pressure that is continuously greater than the normal range is referred to as hypertension. Hypertension is a serious long-term medical condition that dramatically raises the risks of developing heart, brain, kidney, and other problems [15]. The majority of cases have high blood pressure due to nonspecific lifestyle (such as smoking, alcohol, excess salt in the diet, etc.) and genetic factors [16]. Systolic and diastolic pressures combine at the arterioles, where blood pressure falls even further. Blood pressure in capillary networks ranges from between 12 and 15 mmHg at the venous end and 30 to 35 mmHg at the artery end. This is high enough to allow for filtration while remaining low enough to prevent capillary rupture. The pressure falls even further as blood passes through veins, and as blood enters the right atrium, it becomes zero in the caval veins.

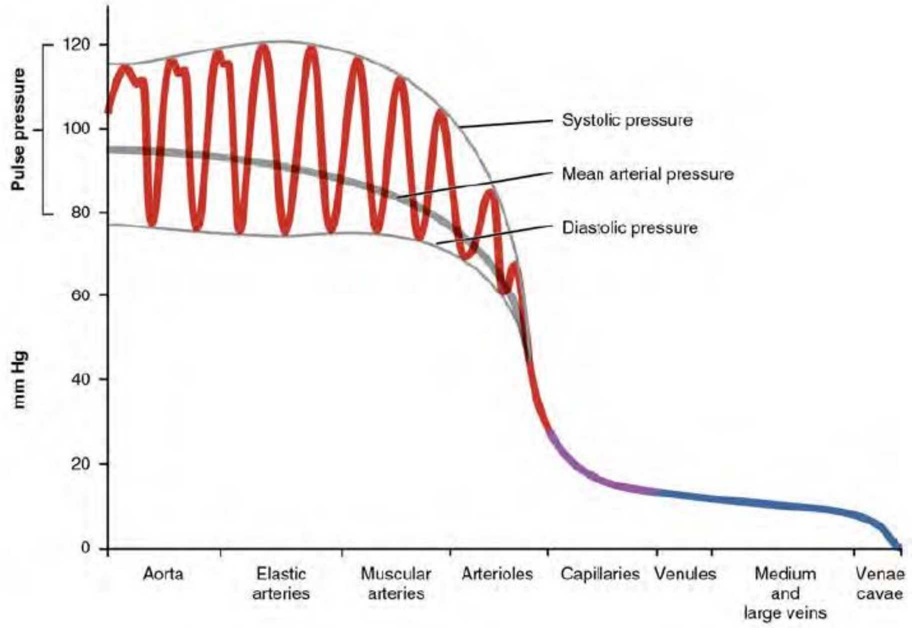

Figure 2.6: Blood pressure in relationship to blood vessels [9].

This difference in pressure at different points in the body generates a gradient of pressure that is the driving force of the blood flow, defined by Poiseuille's equation [17] as:

$$Q = Bloodflow = \frac{\Delta p}{R} = \frac{Gradient of Pressure}{Resistance} \tag{2.1}$$

where R is the resistance in blood vessels, defined as:

$$R = \frac{8L\eta}{\pi r^4} \tag{2.2}$$

where L and r are respectively the lengths and the inner radius of the vessel, and η is the viscosity of the blood. Vasoconstriction and vasodilatation can only significantly alter the radius, whereas changes in the length of the vessel and viscosity occur gradually.

The average pressure of blood in arteries, or mean arterial pressure (MAP), is a significant pressure to monitor.

$$MAP = (CO * R) + CVP \tag{2.3}$$

where CO represents the cardiac output (i.e. the blood flow in one minute), R is the resistance defined in the formula (2.2) and CVP is the central venous pressure (typically around 2-8 mmHg). When the CVP reaches the vena cava, it becomes 0 mmHg and so the MAP can be approximated to the pressure gradient [18].

2.1.3 Blood vessels

The size of blood vessels and the direction of blood flow, either from the heart to the tissues or from the tissues to the heart, are used to classify them. Blood travels through a cavity inside of them called a lumen. The endothelium, an epithelial tissue, is subsequently placed over the lumen. There is a third wall between the two, the thickness and makeup of which depend on the vessel. With the exception of capillaries, the walls of all vessels are constructed from fibrous and elastic connective tissue and smooth muscle tissue. High elastic resistance to the walls, which can contract and release depending on the pressure within, is ensured by the presence of elastin. Contrarily, collagen enables the tissue to lie down without rupturing.

There are five different types of vessels: arteries, arterioles, capillaries, venules and veins. An artery is a blood vessel that leaves the heart and separates into smaller and smaller vessels. The tiniest arteries, called arterioles, eventually split off to form tiny capillaries, which are where wastes and nutrients are exchanged. After that, veins, which are bigger blood vessels that return blood to the heart, are produced from the microscopic blood vessels known as venules. The systemic circuit and the pulmonary circuit are two separate circuits in which veins and arteries move blood. The body's tissues receive oxygen-rich blood from the systemic arteries. Because the majority of the oxygen carried by the arteries has already reached the cells, less oxygen is present in the blood that is returned to the heart through systemic veins. However, in the pulmonary circuit, arteries only carry blood with low oxygen levels to the lungs for gas exchange. The pulmonary veins then carry the freshly oxygenated blood from the lungs back to the heart, where it is pumped into the rest of the body.

The walls of arteries and arterioles are thicker than those of veins and venules because they are located closer to the heart and receive blood that is flowing at a considerably higher pressure [9]. The blood pressure is maintained as it travels through the body thanks to smaller artery lumens than veins. By the time the blood has entered venules and gone through

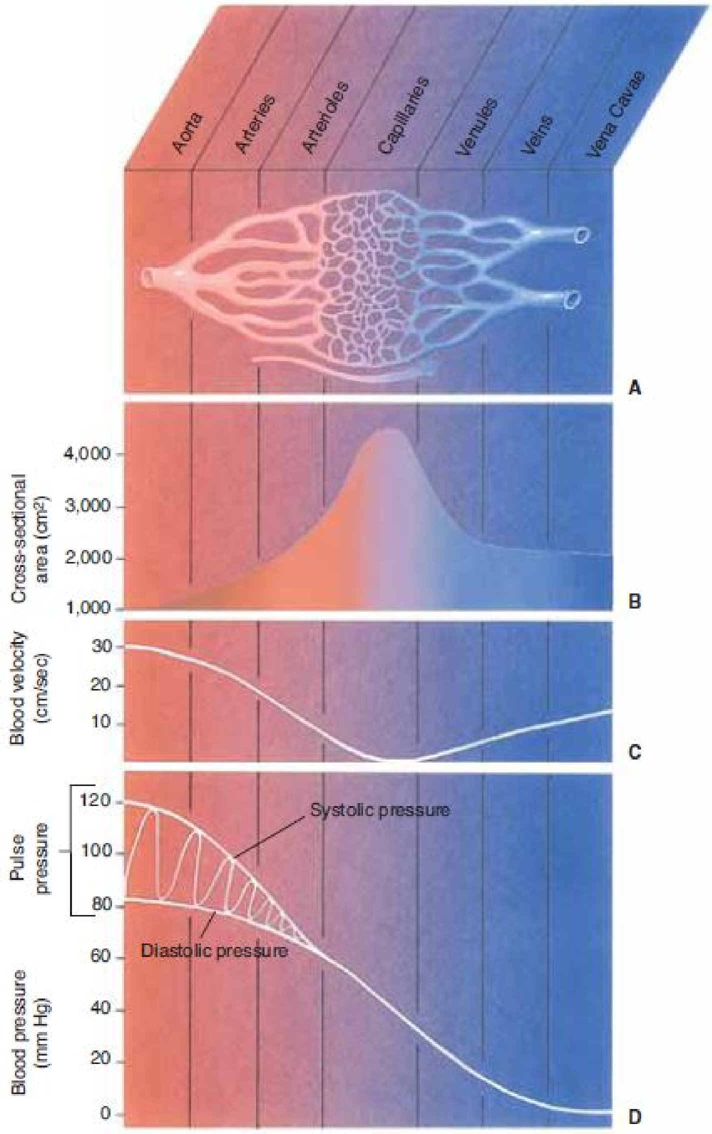

Figure 2.7: Parameters related to blood vessels [7].

capillaries, the pressure that the heart contractions initially applied to it has decreased. As a result, venules and veins are substantially less capable of withstanding blood pressure than arteries are. Their walls are significantly thinner and their lumens are larger, which reduces resistance and allows more blood to flow through the veins. A lot of the body's veins, particularly those in the limbs, also have valves that direct blood flow in one way, toward the heart.

2.2 Arterial Pulse

Because a pulse wave is produced when the left ventricle contracts, the arterial pulse, a crucial physiological characteristic, is defined as a measurement of the heart's rate of contraction. Due to their elasticity, the arteries will constrict after they have expanded, causing the blood to flow to the capillaries and the vein. The arteries contract in reaction to this contraction and volume rises. Due to the arterial pulse being synchronized with heart rate, this expansion and recoiling effect, also known as the pulse, can be palpated manually or recorded electronically to provide information about a patient's health [19]. The measurement is in beats per minute. In a clinical setting, the pulse's strength and rate are both significant. Physical exertion or other short-term events can raise or alter pulse rates, but they can also be signs of a cardiac problem. The intensity of the pulse reflects the force of the heart contraction and output. Systolic pressure will be high if the pulse rate is high. Medical intervention may be necessary if it is weak because the systolic pressure has decreased.

From the arterial pulse waveform, several clinical parameters can be obtained, much more than what the mean artery pressure, systolic and diastolic measurements can show.

2.2.1 Pulse Morphology

The structure of a pressure signal throughout the course of a single cardiac cycle is referred to as pulse morphology [20]. The waveform, shown in Figure 2.8, can be divided in five components:

1. *Systolic upstroke*: it is the rising edge of the waveform. This rising is generated by the ventricular ejection, with a consequent peak of aortic blood flow at the opening of the aortic valve. A slow slope of the rising edge is an indicator of aortic stenosis [21]; The systolic component of the waveform is associated with the R wave of the ECG [19], with a delay between the two waves;

2. *Systolic peak pressure*: it is the maximum pressure produced during the ventricular systole. The peak is much higher as the collecting site is

far away from the heart because the pressure increases and the vessels' resistance decreases. The shape of the peak derives from the influence of reflected waves generated into the vascular system. In fact, pulse waves are usually forced back to the aortic valve causing in some cases even an "anacrotic notch" along the systolic upstroke, depending on the collection site: in fact, it is more evident on the carotid artery instead of the peripheral arteries. The systolic peak of the waveform is also associated with the R wave of the ECG [19], with a delay due to the transmission time of the pressure wave to the collecting site;

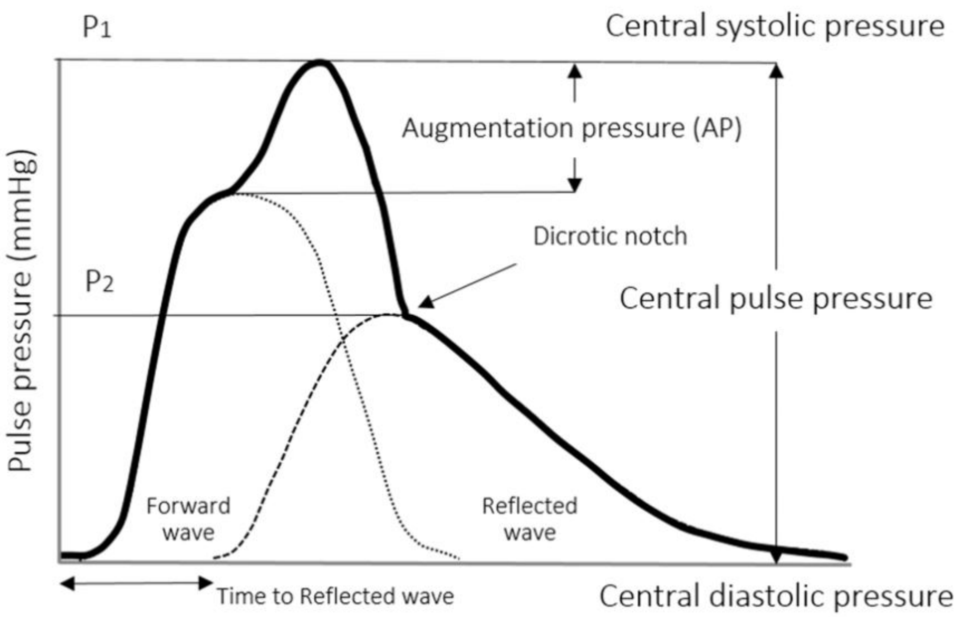

Figure 2.8: Arterial pulse waveform [22].

3. *Systolic decline*: it corresponds to the end of systole by the heart, with a rapid drop in pressure;

4. *Dicrotic notch*: it is caused by the closure of the aortic valve, corresponding to the start of diastole, that causes a sharp increase of pressure during the falling edge of the waveform;

5. *Diastolic runoff*: it is the decrease in pressure that occurs after the aortic valve closes. The pressure inside the aorta gradually drops exponentially when the ventricle stops pumping blood there. This phenomenon occurs

thanks to the artery's flexibility, which keeps the early diastole pressure high and forces blood into the systematic circulation [21].

There are other several parameters that can be extrapolated from the pressure waveform. For example, the *systolic amplitude*, i.e. the height of pulse, is connected to vascular distensibility: a low amplitude corresponds to vasoconstriction or a decrease of blood volume and a high amplitude denotes vasodilatation or an increase of blood volume [23], so it can be used as an indicator for blood volume. Additionally, vascular resistance can be related to the pulse width at the half height of the systolic peak. It is also possible to use the *area under the curve* (AUC) to estimate the mean arterial pressure (MAP), used as an indicator of tissue perfusion. Finally, The difference between the dicrotic notch peak (AP2) and the systolic pressure peak (AP1), reported as a percentage of the pulse pressure, is known as the *augmentation index* (AIx):

$$AIx = (\frac{AP1 - AP2}{AP1}) * \frac{1}{100} \tag{2.4}$$

It is utilized to forecast hazardous cardiovascular events (for example as the gold standard parameter for diagnosis of hypertension) [22]. An rise in the augmentation index will give an assessment of the stiffness of the arterial system; a high augmentation index is associated with a number of vascular diseases, including migraine, diabetes, and arrhythmia.

2.2.2 Collecting Sites

Arterial pulse can be collected on different sites in the body, both close to the heart and far from it. Sites near the heart are at the carotid artery, the brachial and the femoral ones, while the peripheral sites correspond, for example, to the radial or the tibial artery.

Moving the collecting site away from the heart, there are some differences between their pulse:

- the amplitude of the pulse grows straying away from the heart, accompanied by a sharp rising of the systolic upstroke, because of the high resistance of small arteries [19];
- the dicrotic notch becomes lower in amplitude and the phenomena that generate it take place with more delay compared with the systolic peak pressure.

In Figure 2.9 below, the differences in amplitude and morphology of the arterial pulse registered in different collecting sites are shown.

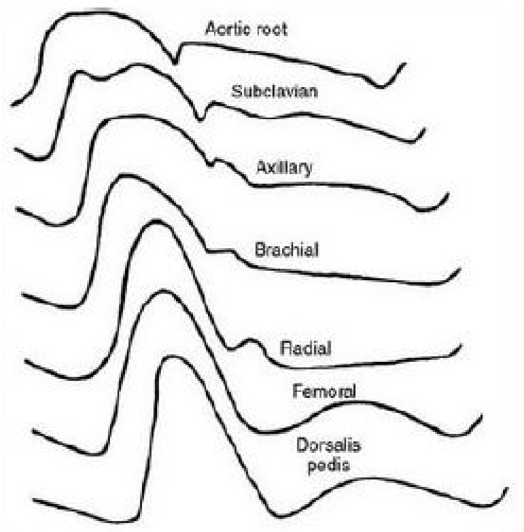

Figure 2.9: Differences in pulse wave among different collecting sites [24].

2.3 Pulse Wave Velocity

After the acquisition of the pulse wave, it is possible to calculate the *Pulse Wave Velocity* (PWV), a parameter defined as the speed at which the pressure wave generated from the systole spreads from the aorta to the peripheral arteries [22]. To calculate the value of PWV, it is necessary to measure firstly the distance on the skin between the two collecting points, known as pulse wave distance (PWD); after which, the elapsed time for the pulse wave to transit between sites is measured and is called pulse transit time (PTT). Dividing the pulse wave distance by the pulse transit time, the value of PWV is obtained.

It has been demonstrated in literature over the years that the gold standard for the PWV assessment is to consider the carotid and the femoral artery as collecting sites of signal [26][27]. Clinically, two methods to estimate this parameter are used:

- *One-step method*: the pulse wave is detected concurrently from the carotid and the femoral artery, obtaining directly the value of PTT;

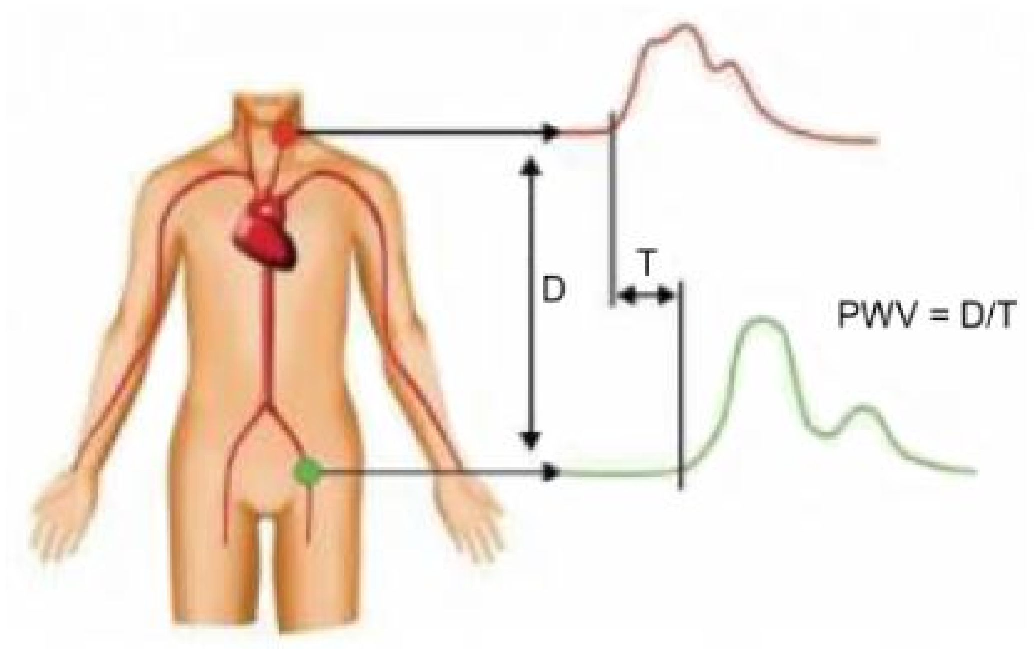

Figure 2.10: Example of PWV measurement [25].

- *Two-step method*: two different propagation times are measured. Firstly, it is measured the time needed to propagate the pulse wave from the heart to the carotid artery, known as carotid PTT (or cPTT); after that, the elapsed time for the wave to propagate from the heart to the femoral artery (femoral PTT or fPTT) is measured. The value of PTT is so calculated by subtracting the two values just measured [4]. For this method, an ECG recording is needed because the R-peak is used to synchronize the two waveforms [28].

The arterial stiffness of the artery between the two measurement sites is thought to be measured by PWV. It rises proportionately to arterial stiffness and is controlled by the geometric and elastic characteristics of the arterial wall. This behavior can be described by utilizing the Moens-Korteweg equation to calculate PWV, which links it to a measurement of the stiffness of an elastic artery and was developed as early as 1878 [29]:

$$PWV = \sqrt{\frac{Eh}{2r\rho}} \tag{2.5}$$

where E is Young's elastic modulus of the arterial wall, h is the arterial wall thickness, r the end-diastolic radius of the artery, and ρ the blood density. Later on, Bramwell and Hill [30] demonstrated the relationship of the PWV with the relative change in aortic volume *($\Delta V/V$)* and pressure (*(ΔP)*:

$$PWV^2 = \frac{V\Delta P}{\rho\Delta V} = \frac{1}{distensibility} \tag{2.6}$$

with the distensibility defined as a metric of the blood vessels stiffness [31]:

$$Distensibility(D) = \frac{d_{systole} - d_{diastole}}{(P_{systole} - P_{diastole})d_{diastole}} \tag{2.7}$$

where d and P are the diameter and blood pressure of the vessel during systole and diastole respectively. According to these formulas, a higher value PWV is clearly related to higher arterial stiffness, with lower distensibility and compliance. If the arterial stiffness increases, the aortic pulse pressure and also systemic pressure increase too, with less blood filling the ventricle during diastole. Only in recent years, the PWV is taken into consideration as a valid parameter for diagnosing cardiovascular disease risks, like arteriosclerosis, hypertension, and heart failure.

For a healthy subject, a typical value of PWV oscillates between *6.6 m/s* for subjects with less than 30 years and *11.7 m/s* for people who have more than 70 years [32].

Age category (years)	Blood pressure category				
	Optimal	Normal	High normal	Grade I HT	Grade II/III HT
PWV as mean (±2 SD)					
<30	6.1 (4.6–7.5)	6.6 (4.9–8.2)	6.8 (5.1–8.5)	7.4 (4.6–10.1)	7.7 (4.4–11.0)
30–39	6.6 (4.4–8.9)	6.8 (4.2–9.4)	7.1 (4.5–9.7)	7.3 (4.0–10.7)	8.2 (3.3–13.0)
40–49	7.0 (4.5–9.6)	7.5 (5.1–10.0)	7.9 (5.2–10.7)	8.6 (5.1–12.0)	9.8 (3.8–15.7)
50–59	7.6 (4.8–10.5)	8.4 (5.1–11.7)	8.8 (4.8–12.8)	9.6 (4.9–14.3)	10.5 (4.1–16.8)
60–69	9.1 (5.2–12.9)	9.7 (5.7–13.6)	10.3 (5.5–15.1)	11.1 (6.1–16.2)	12.2 (5.7–18.6)
≥70	10.4 (5.2–15.6)	11.7 (6.0–17.5)	11.8 (5.7–17.9)	12.9 (6.9–18.9)	14.0 (7.4–20.6)
PWV as median (10–90 pc)					
<30	6.0 (5.2–7.0)	6.4 (5.7–7.5)	6.7 (5.8–7.9)	7.2 (5.7–9.3)	7.6 (5.9–9.9)
30–39	6.5 (5.4–7.9)	6.7 (5.3–8.2)	7.0 (5.5–8.8)	7.2 (5.5–9.3)	7.6 (5.8–11.2)
40–49	6.8 (5.8–8.5)	7.4 (6.2–9.0)	7.7 (6.5–9.5)	8.1 (6.8–10.8)	9.2 (7.1–13.2)
50–59	7.5 (6.2–9.2)	8.1 (6.7–10.4)	8.4 (7.0–11.3)	9.2 (7.2–12.5)	9.7 (7.4–14.9)
60–69	8.7 (7.0–11.4)	9.3 (7.6–12.2)	9.8 (7.9–13.2)	10.7 (8.4–14.1)	12.0 (8.5–16.5)
≥70	10.1 (7.6–13.8)	11.1 (8.6–15.5)	11.2 (8.6–15.8)	12.7 (9.3–16.7)	13.5 (10.3–18.2)

Figure 2.11: Distribution of pulse wave velocity (PWV) values (m/s) in the reference value population (11 092 subjects) according to age and blood pressure category [32]. *(SD = standard deviation, 10 pc= upper limit of 10th percentile, 90 pc = lower limit of the 90th percentile, HT = hypertension)*

2.3.1 Clinical devices for PWV estimation

Mostly of commercial devices carry out PWV estimation using regional or local measurements, of which the most used is the regional one.

The regional PWV measurement is typically carried out at two distinct collecting sites, such as the carotid, radial, or femoral artery. It enables the estimation of the average PWV over a significant portion of the arterial tree. Due to the considerable distance between the two sites, arteries with diverse mechanical properties are taken into consideration, which explains why early modest differences in stiffness are difficult to notice. Additionally, the distance must be measured externally, which contributes to a sizable inaccuracy in the PWV calculation.

Local PWV measurement, instead, is performed on a brief part of the same artery and it is not affected by the disadvantages of the regional measurement.

Most of the commercial devices currently used in clinical have optimal performance and accuracy, but the disadvantages of their use are the high costs of the devices and their operator dependence, which have a high impact on the accuracy and the repeatability of the measurements. Last, but not least, some of them are not based on wireless or Bluetooth systems, so there is also the encumbrance of wires. To overcome these problems, this thesis aims to find and develop a Bluetooth, non-invasive and low costs device for PWV estimation.

SphygmoCor® SphygmoCor® is the global gold standard device for assessing the shape of the pulse and the stiffness of the arteries with the measure of the PWV. It is developed and produced by the AtCor Medical [33] and tonometers are used as sensors. It performs the measure of the PWV with the two-step method previously described (with the use of ECG's R-peak for synchronization); in addition, it measures brachial systolic and diastolic pressure, and aortic systolic blood pressure.

PulsePen PulsePen is a non-invasive wireless device, developed by DiaTecne [34], which uses tonometers (inserted in a pen support) as sensing elements. It performs the two-step method for PWV evaluation and it additionally evaluates central blood pressure and pulse wave analysis.

Figure 2.12: *SphygmoCor [33].*

Figure 2.13: *PulsePen [34].*

2.4 Utilized Devices

The aim of this thesis is to find an alternative to the tonometers used in the ATHOS prototypal system [4] because these sensors are prototypical, not commercial and so they depend too much on their manufacturer. So, the first period of the thesis has been dedicated to the search in the market for all the load cells or force sensors. In particular, the research was focused on all sensors that measure the force (due to the displacement of the artery during pulse) which have small dimensions, low costs and a small force range to detect. Finally, the choice has fallen on the FMA MicroForce Sensor, produced by Honeywell, a digital load cell which has all the features we were looking for.

2.4.1 FMA MicroForce sensors

The piezoresistive-based force sensors in the FMA Series are capable of measuring force utilizing a digital output over the specified full-scale force span and temperature range. They are properly calibrated and temperature compensated for sensor offset, sensitivity, temperature effects, and non-linearity using an onboard application-specific integrated circuit [35]. In direct proportion to the force exerted on the mechanically connected stainless steel sphere, they provide a stable output; the sphere is mounted directly over a silicone sense die located on top of the sensor as shown in Figure 2.15. The optimal performance is reached when the force is applied along the vertical axis to the top centre point of the coupling sphere. A reproducible performance and a dependable mechanical link to the application are provided by direct mechanical coupling, which makes it simple to interface with the sensor.

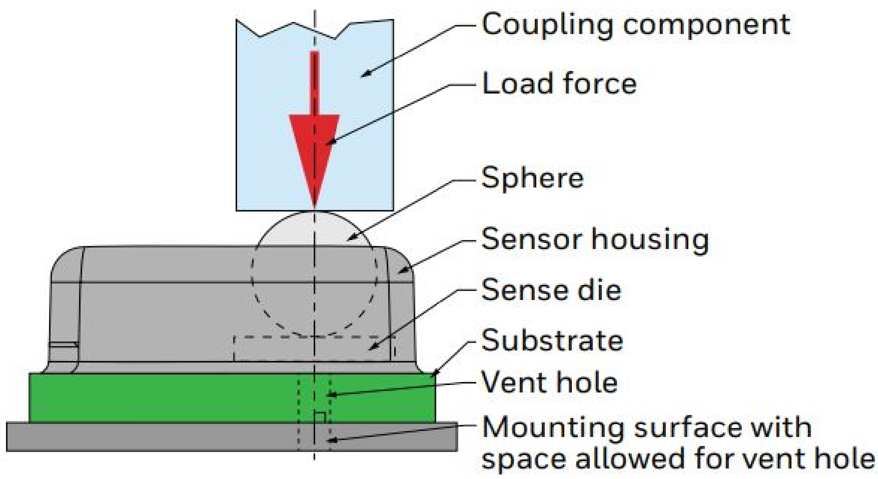

Figure 2.14: Structure of the sensor, with the optimal alignment of load force [35].

The small form factor (5 mm x 5 mm for the base, 2.15 mm for the height), low power consumption (about 14 mW) and low costs make it an ideal solution for the thesis aim. The sensing area is the sphere on the top of the sensor: it has a diameter of 1.6 mm and a height that can variate between 0.293 mm and 0.483 mm, depending on the sensor force range. It is necessary to be careful of the over-application of force: indeed, the maximum overforce this sensor can withstand is three times its force range. A continuous overforce exposure may cause permanent damage to the sensor, rendering it no longer usable.

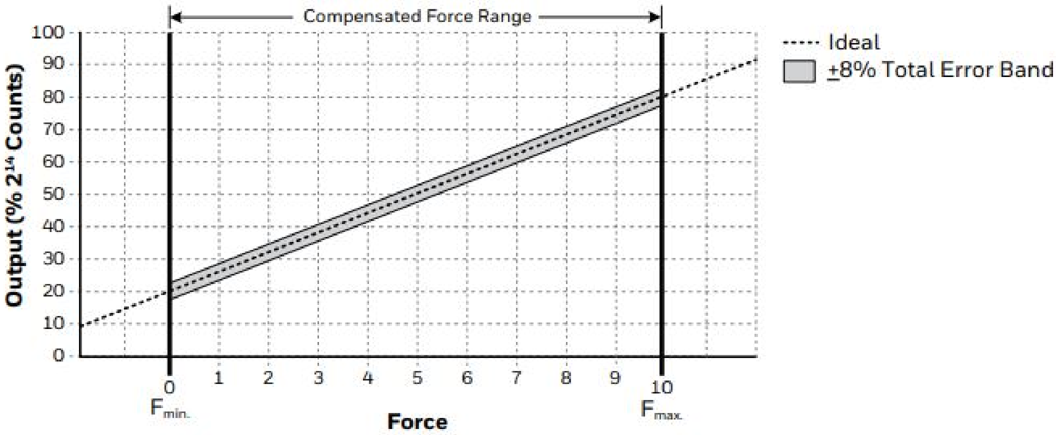

Figure 2.15: Optimal range of use of the sensor [35].

The model of sensor chosen is the *FMAMSDXX005WCSC3*, where the acronym explains its characteristics: more specifically, it is a compensated and amplified sensor *(A)*, with mechanical coupling *(M)* and a sphere as contact element *(S)*; it also permits to determine if the sensor is working correctly with a diagnostic function (*D*). It has different force ranges (*005, 015, 025*) respectively 5, 25 and 25 Newton which allows the user to select the best range for its application to maximize sensitivity and resolution, with the best results achieved as close as possible to full scale. For the force involved in this application, sensors with a force range of 5 and 15 Newton have been chosen to be tested. As said before, this sensor has a digital output, compatible with the Serial Peripheral Interface (SPI) communication (*S*) and it needs a power supply of 3.3 V (*3* at the end of the acronym).

The six pads for the electrical connection are located on the bottom of the sensor, where they can be soldered with an acquisition system for

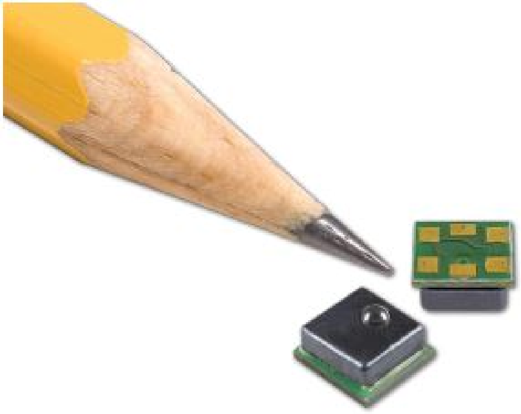

Figure 2.16: *Comparison between an FMA sensor and a pencil tip [35].*

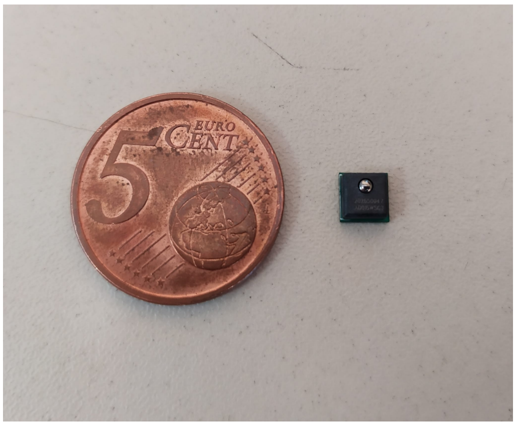

Figure 2.17: *Comparison between an FMA sensor and a five-cent coin.*

processing sensor data output. A round adapter has been realised to align these pads scheme to the trails on the PCB of the ATHOS system which will be explained in detail in Chapter 5.

2.4.2 ATHOS System

The ATHOS system is an experimental device developed by the MiNES research group in Politecnico di Torino, performing the PWV estimation with the one-step method using tonometers. The sensing elements of the tonometers are the piezo-resistive and ultra-compact MEMS nano pressure sensor LPS22HB, produced by STMicroelectronics [6], which works as a digital output barometer, with a sensing range between 260 and 1260 kPa. Thanks to the addition of resin in correspondence with the sensitive element, the sensor has been converted into a force sensor.

The tonometers are integrated into two ergonomic probes for easy handling and, thanks to a Bluetooth Low Energy (BLE) connection, they send data directly to a laptop [5]. They are displayed in real-time on a graphical interface where parameters like PTT or instant PWV are calculated and displayed. This system is the second version of a previous prototypal system developed previously [4] where the Bluetooth data transmission didn't take place directly between the probes and the laptop, but the probes were connected with wires to the main unit that collects the two pulse waves and an electrocardiogram signal (ECG) and subsequently sent them to the laptop.

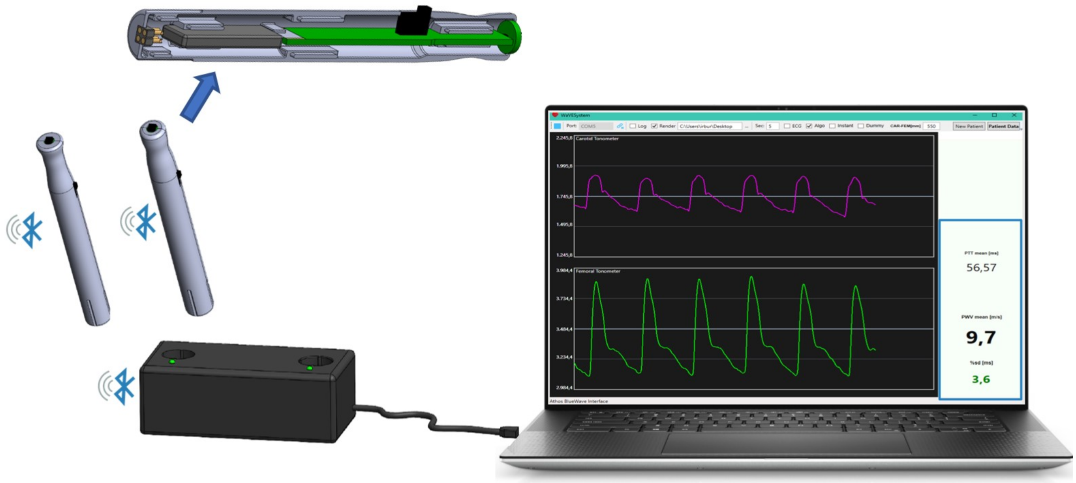

Figure 2.18: Overview of the system with probe details [5].

The components of the ATHOS system Printed Circuit Board (PCB) will be analyzed more specifically in Chapter 5, along with some notions about Bluetooth Low Energy, a description of the probe holder and the way the data exchange between sensors and laptop take place.

2.5 Utilized Software

MATLAB MATLAB R2022a MATLAB is a C-based environment developed by MathWorks that contains the same-named high-level programming language that is used for numerical calculation and statistical analysis. The software has been used for filtering, analysing and comparing all the acquired arterial pulse signals and for computing the PWV values.

SolidWorks SolidWorks is a parametric three-dimensional drawing and design software, manufactured and marketed by Dassault Systèmes. It has been used to design the support for the characterization of the load cell, the pen-shaped support for acquiring data from patients and the recharge station. The drawn supports have been printed using Form3, a resin 3D printer, with the use of FormLabs, a software that allows the placement of the 3D models on the printer platter.

STM32CubeMX STM32CubeMX is a graphical tool provided by STMicroelectronics that allows for simple configuration of STM32 microcontrollers and ST Boards as well as step-by-step development of initialization C code for the Arm Cortex-M core. The first step consists in selecting either an STMicroelectronics STM32 microcontroller or an ST Board; then the second step allows the configuration of the peripherals (like GPIOs, USART, SPI), the clock setup for the whole system and the middleware stacks (USB or TCP/IP). In the thesis, STM32CubeMX has been used for the initialization of the utilized peripherals, the clock of the system and to generate the initialization C code.

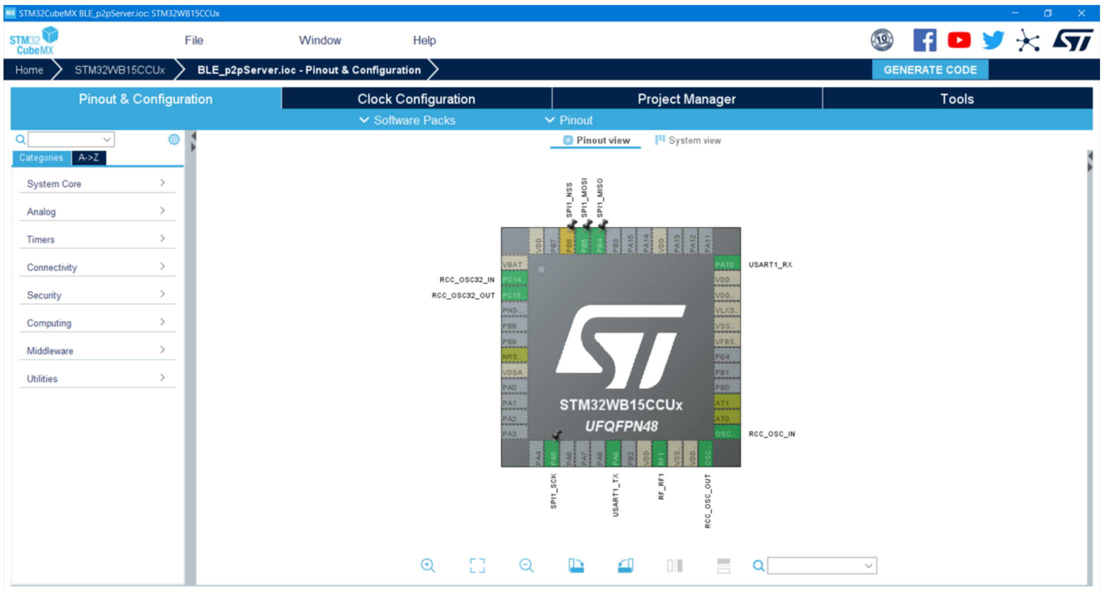

Figure 2.19: Initialization of microcontroller parameters and tools in the STM32CubeMX environment.

LabVIEW LabVIEW (Laboratory Virtual Instrumentation Engineering Workbench) is the integrated development environment for National Instruments' visual programming language, called G language, which has a graphical syntax. Icons and other graphical objects, joined by wires, define data structure and algorithms to form a kind of flowchart. It has been used to create a Graphic User Interface (GUI) to plot and visualize data in real-time transmitted by the sensor using the UART protocol.

Keil uVision 5 Keil uVision 5 is an IDE (Integrated Development Environment) for C/C++ codes developed by Arm Keil. It has been used to program the data acquisition from the sensor and their transmission to the computer using the USART protocol at the beginning and after using BLE (Bluetooth Low Energy) Transmission.

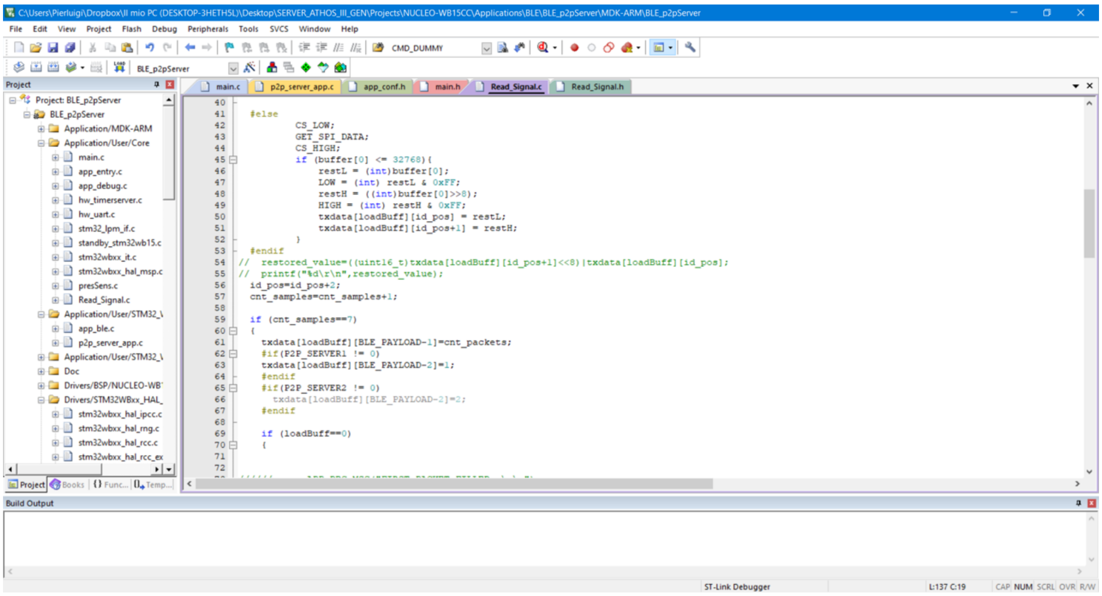

Figure 2.20: Keil IDE environment.

PuTTY PuTTY is an SSH, Telnet and client combined with a terminal emulator for remote management of computer systems. It allows for example control of remote servers and serial ports (COM). It has been used for reading data which the microcontroller sent on the serial port of the laptop and to save them in a text file.

STM32CubeProgrammer STM32CubeProgrammer is a software tool developed by STMicroelectronics which enables reading, writing, and verifying device memory in a simple environment. Additionally, a variety of features are available for programming STM32 internal memories (such as Flash, RAM, and OTP). It has been used to upload the BLE stack code on the microcontroller STM32WB15CC mounted on the PCB of the ATHOS system that manages the real-time Bluetooth data transmission between the sensor and the dongle inserted in the computer.

Visual Studio 2022 Microsoft Visual Studio 2022 is an integrated development environment (IDE) developed by Microsoft which supports multi-programming languages. It allows the creation of a graphic user interface (GUI), add-ons, console, etc. It has been used to create a GUI that allows the real-time visualization of data collected by sensors and saves them on the computer for future elaboration.

Altium Designer Altium Designer is an electronic and PCB (Printed Circuit Board) design automation software package for printed circuit boards developed by Altium Limited. It has been used to design the round adaptor used to conform the sensor footprint with the tracks on the ATHOS PCB.

Chapter 3

Load Cell Sensor configuration

This chapter provides an overview of the Serial Peripheral Interface (SPI) communication, used to interface with sensors. After data from the sensor are analyzed, the algorithm implemented for reading the sensor is described. In the end, a first graphic interface in LabVIEW is provided, used for the real-time visualization of data flow from the sensor.

3.1 SPI communication

Serial Peripheral Interface (SPI) indicates a high-speed synchronous serial communication system between a microcontroller, called *Master*, and one or more peripherals, called *Slave* (which can be other microcontrollers, integrated circuits, etc.) which are selected via hardware. It is very useful because it allows faster speeds than other protocols like UART (Universal Asynchronous Receiver-Transmit) or I2C (Inter-Integrated Circuit). In the thesis, this protocol is needed to interfacing with the digital sensor.

The communication between the master and one or more slaves occurs through four communication lines:

- Serial Clock (SCLK or SCK): driven by the master, it is needed to synchronize the data exchanged to the rising or falling of the edge of the internal clock of the microcontroller. A bit is sent for each clock cycle;
- Chip/Slave Select (CS or SS): it is used to select the slave to communicate

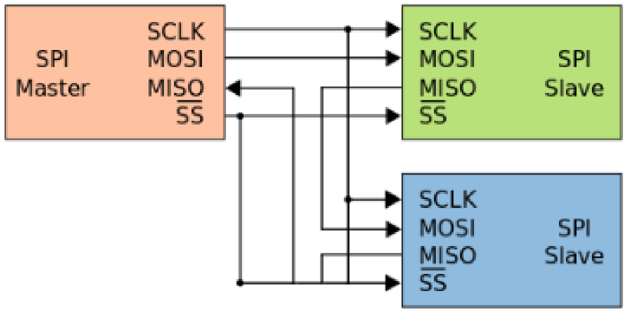

Figure 3.1: SPI communication between a Master and a single Slave.

with. Normally, the pin used as CS is maintained at a high logic level and it is taken to the logical low level during master and slave communication;

- Master In Slave Out (MISO): it is the line through which the slave sends data to the master;
- Master Out Slave In (MOSI): it is the line through which the master sends data to the slave. Normally, it is used for sending commands to the peripheral or to set bits in registers for the next reading operations.

In this thesis, there is no need for the MOSI line because the micro force sensor has an easy reading system that does not require particular commands from the master, it only needs to be queried by the master and it will provide the measurements that it performs.

3.2 Data reading and transmission to laptop

Initially, the firmware has been developed using C/C++ language and loaded on a Nucleo board STM32L452RE [36], produced by STMicroelectronics, to find the right sampling rate at which read data, to perform the first sensor readings, to carry out cycles of characterization of the load cell (described in chapter (4)) and to obtain some pulse wave signal.

Thereafter, the firmware has been transferred on a Nucleo board [37] STM32WB15CC, which includes Bluetooth transmission drivers and tools because the acquisition system has to be transferred on the Bluetooth version of the ATHOS prototypical system instead of tonometers.

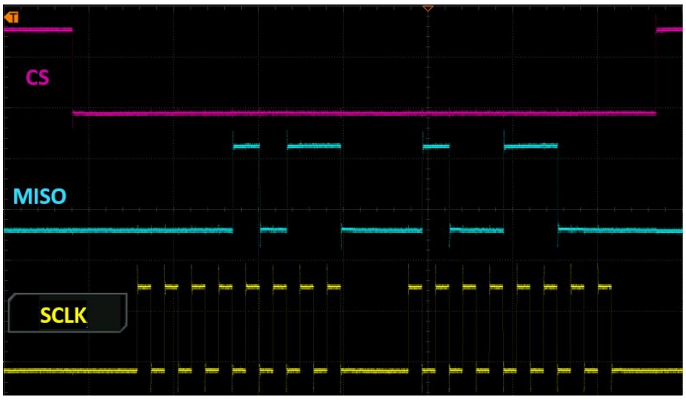

Figure 3.2: Visualization of the SPI communication between the microcontroller and the sensor, using an oscilloscope to check the logic level of pins.

3.2.1 Nucleo board STM32L452RE

The STM32L452RE Nucleo-64 board is a compact and ultra-low-power board provided by the STM32 that embodies an STM32L452RE microcontroller [36], based on the high-performance Arm® Cortex®-M4 32-bit RISC core operating at a frequency of up to 80 MHz. It has high-speed memories: up to 512 Kbyte of Flash memory and 160 Kbyte of SRAM. It provides six different timers, 1x16-bit ADC (Analog to Digital Converter) channels, 3xSPI, 4 x UART, 1xUSB and 4xI2C peripherals. It has also a temperature sensor and provides a power supply from 1.71 V to 3.6 V.

3.2.2 Sensor data readout

Honeywell digital output force sensors are set up to operate so that data on the MISO bus line transitions during the falling edge of clock pulses, which means that the Master device should sample this at the rising edge of the clock pulse. This sensor allows different types of readouts:

- *Two-Byte Data Readout*: the first two data bytes read are the compensated force output (14 bits), along with sensor status bits (2 bits);
- *Four-Byte Data Readout*: in addition to the force output, the other two bytes are the optional compensated temperature output.

For this thesis, the two-byte data readout is performed because temperature measurements are irrelevant to the application case study.

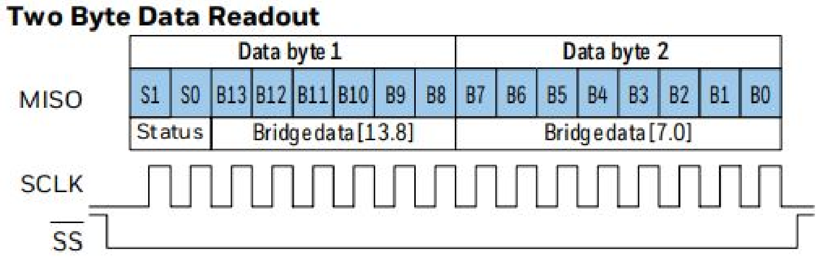

Figure 3.3: Sensor SPI force measurement packets readout [38].

For doing the readout of the sensor, it is necessary to turn the pin of the Chip Select to the low logic level. In the following 16 clock cycles, the acquisition is performed by a simple reading of the sensor output register, so the 16-bit data is received through the MISO line and stored in a temporary buffer. After that, the Chip Select pin is turned to the high level and there it remains until the next acquisition. The timing of the level switch of CS is driven by an internal timer which is set at the sampling frequency chosen (whose choice will be discussed in the next sections). When the set time elapses, the timer generates an interrupt and a specific callback function is executed in which the data acquisition is performed. It has been chosen interrupt mode for acquiring data to not block the microcontroller when the acquisition is performed, so as to have a continuous acquisition and a normal microcontroller functioning.

The two most significant bits of Data byte 1 (S1 and S0 defined in Figure 3.3) are an indicator of the sensor status: this diagnostic state is very important because it allows knowing if the system is working correctly or if there are some problems like short circuits or stale data. In the table 3.1 below are shown the possible combinations of these bits and their meaning.

So, before storing data from the sensor in the laptop, a control condition has been implemented in the firmware just after the data readout: the check is done on the status bits, so only if these bits are equal to "00" the data is sent to the laptop using UART protocol for future elaborations.

The output that the sensor provides has a 14 bits-dynamic that is proportional to the supply voltage (3.3 V), so the output can be expressed as a voltage solving the proportion:

$$output : 2^{14bits} = output_{Voltage} : V_{supply} \tag{3.1}$$

S1	S0	Definition
0	0	Normal operation, valid data.
0	1	Device in command mode (used just for programming the sensor, not seen in normal use).
1	0	Stale data: shows information that has already been retrieved since the last measurement cycle or data. It happens when the sensor cannot update the output buffer as quickly as the master polls the data.
1	1	Diagnostic condition: loss of sense element connection or short circuit of sensing element.

Table 3.1: Diagnostic states in data readout [38].

The digital output can be also expressed with its transfer function [38], where the digital output is defined as:

$$Output = \frac{(Output_{max} - Output_{min}) * Force_{applied}}{ForceRange} + Output_{min} \tag{3.2}$$

where $output_{max}$ is the value of the 90% of the dynamic, $Output_{min}$ is the value of the 10% of the dynamic, $Force_{applied}$ is the force measured by the sensor (in Newton) and *Force Range* is the value of the range of the sensor (in Newton).

Overturning the equation (3.2), from the value of the output read it is possible to calculate the force applied on the sensing sphere (in Newton):

$$Force = \frac{(Output - Output_{min}) * ForceRange}{Output_{max} - Output_{min}} \tag{3.3}$$

These equations have been implemented in post-processing on a MATLAB script, which produces both voltage and force graphs of the output for better visualization and better quantification of the acquired data. This will be discussed in chapter (4).

3.2.3 Algorithm for sampling frequency

On the load cell datasheet, the data readout sampling frequency is not indicated. Without being aware of this parameter, an investigation on a possible sampling frequency has been carried out, starting from a check of the status bits (just described in section 3.2.2) of each data acquired from the sensor.

For the timing of the acquired data, several parameters have been settled on the microcontroller using the tool STM32CubeMX: in addition to the peripherals and other components default initialization are the micro's clock frequency, the Prescaler and the Counter Period Value of the timer used.

A time period of thirty seconds is set in which to acquire data from the sensor, and a check is made on the status bits of each measurement read: if there are incorrect measurements (*"stale data"*) at the end of the time, it means that the sampling rate is too high. It is, therefore, necessary to proceed to lower it by going to act on the micro's clock frequency and the timer settings (Prescaler and Counter Period) to time the acquisitions. In Table 3.2 the steps in frequency are summarized: starting from a sampling frequency of 2kHz, an attempt was made to minimize the number of "stale" measurements in relation to the number of measurements taken in the thirty seconds of acquisition, dependent on the sampling rate in question. It can be noticed that decreasing the frequency also decreases the number of incorrect readouts, due to faster data requests from the microcontroller than the refresh time of the sensor output register.

System Clock [MHz]	Sampling rate [Hz]	"Stale data" (%)
80	2000	18,05% (10830)
80	1000	5.09% (1527)
80	800	0.7% (181)
60	600	0.2% (37)
60	500	0.16% (25)
45	450	0.1% (12)
44	440	0.04% (5)
80	**400**	**0% (0)**

Table 3.2: Summary table of different sampling frequencies tested. The percentages are calculated as the stale measurements in relation to the total measurements acquired in 30 seconds. In parenthesis the number of wrong measurements for each frequency.

At the end of the investigation, 400 Hz is chosen as the sampling rate of the system because it is the highest sampling rate possible at which there is 100% of correct data. For setting this sampling rate, the system clock is set to 80 MHz, with a Prescaler value of 20000 and a counter period value of 10. With this combination the timer generates an interrupt every 25 ms, going to execute the function that queries the load cell for acquisition.

After the choice of the sampling rate, several acquisitions have been carried out. To save all the measurements, data just taken from the sensor are sent via UART protocol to the laptop and visualized in real-time using the software Putty, which allows the visualisation and saves raw data that arrive on the serial port of the laptop (COM port). Alternatively, for graphic visualization of the pulse wave, a LabVIEW basic Graphic User Interface (GUI) has been implemented with a real-time plotting of data read from the COM, implementing also a real-time post-processing filtering stage (showed more in detail in section (3.2.4)).

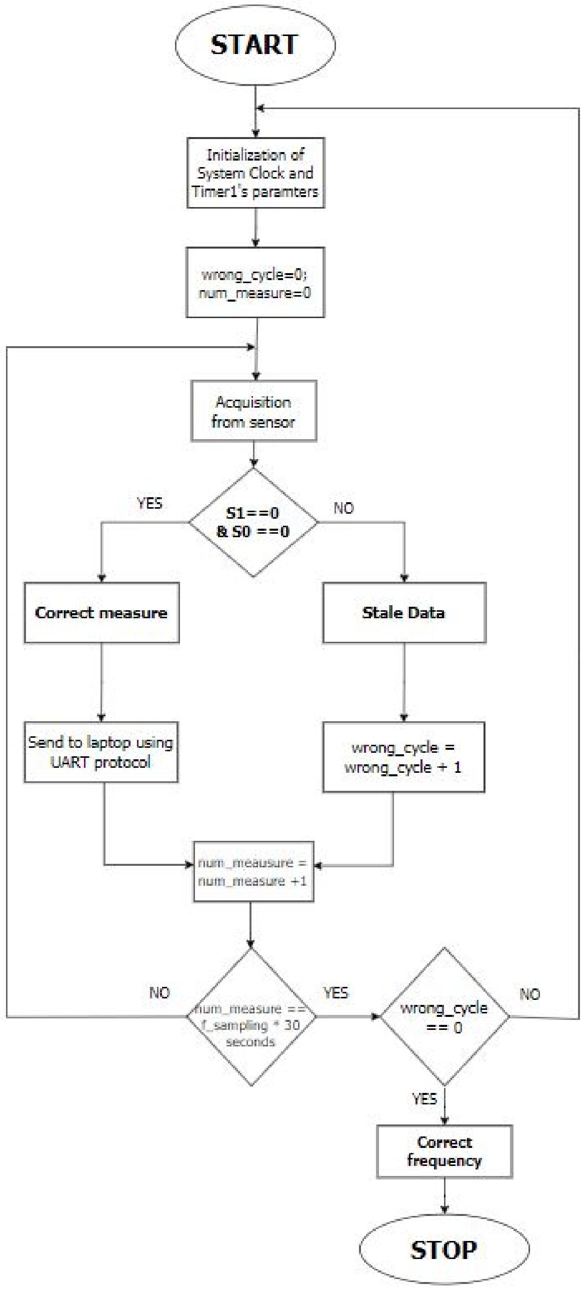

Figure 3.4: Flow chart of the sampling frequency algorithm.

3.2.4 LabVIEW Interface

The use of the software LabVIEW has been relevant to watch and analyze if the sensors used are working correctly, producing an output signal that is similar in morphology to the pulse one. Using its tools and block diagrams, a basic GUI has been implemented: basically, it reads sensor data from the COM serial port, performs the transformation in a voltage measurement using the equation (3.1) and displays them in a real-time chart. Moreover, the signal has required to be filtered because it has shown a low resolution, resulting in a bad visualization and in the impossibility to extract further the parameters needed for the PWV estimation. So, the filtering stage has been implemented using a band-pass filter of the 4^{th} order between the cutoff frequencies of 0.1 Hz and 10 Hz; the raw data read are filtered in parallel with their raw display and then plotted in a second graph to highlight a clear pulse waveform.

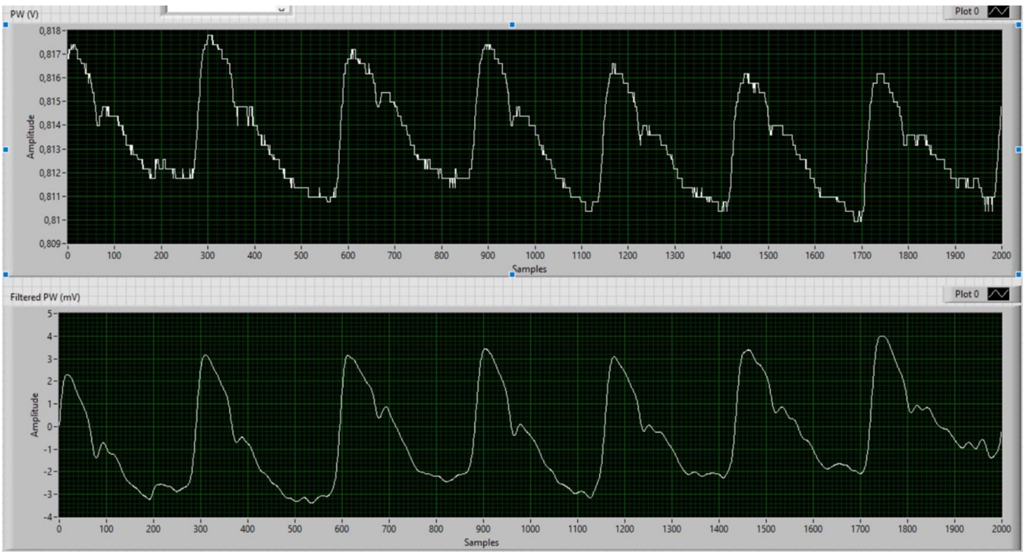

Figure 3.5: LabVIEW real-time interface. In the upper chart, raw data from the sensor are plotted; in the bottom graph, the signal shown has been filtered before plotting.

The filters available on LabVIEW are not as accurate as the processable filters of special data processing software, like MATLAB for example; so later, the post-processing stage has been implemented on MATLAB for a more precise filtering action. The same filter (a Chebychev band-pass of the 4^{th}

order between 0.1 Hz and 10 Hz) used on LabVIEW has been implemented.

3.3 Global flowchart

Here the global flowchart of the implementation just described is shown, for a 400 Hz sampling rate, with all the steps performed for a correct readout and a good visualization. Control over the acquired data from the sensor is always carried out even if the sampling frequency chosen is low enough to query the load cell without there being a risk of stale data.

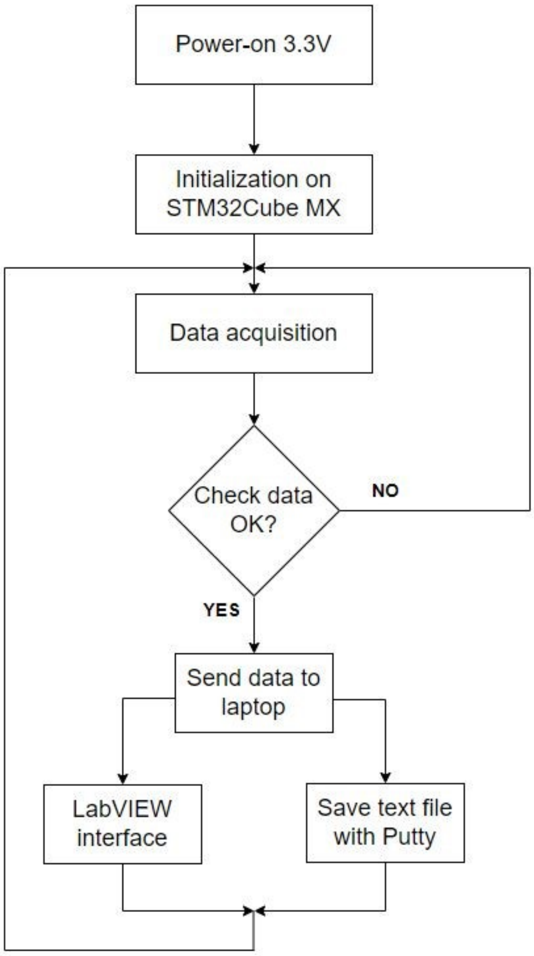

Figure 3.6: Global flowchart of the firmware implementation.

Chapter 4

Characterization and first measurements

In this section the characterization of the sensor is provided, starting from the design of the support to the measurement cycles done. In the end, the description of the first draft of the sensor pen holder is provided, among with some signals acquired.

4.1 Support 3D design

As mentioned in Chapter 2, two different sensors have been taken into account, one with a force range of 5 N and the other one with 15 N. These are the lowest force ranges available for this type of sensor and they are suitable for the thesis application because the displacement of the carotid or femoral artery generates a force of a few Newtons. At first, the sensor was soldered onto a rectangular PCB with a header for each pad coming out of it because it was intended to be tested on a breadboard. This PCB has the pad layout coincident with the pad layout present below the sensor. The vias on the bottom are soldered with headers so they can be mounted on breadboards and connected to the microcontroller to acquire data.

The characterization aimed at choosing which sensor is more suitable for the thesis purpose. Calibration weights were used to carry out the characterization; they are employed in laboratories as sample weights because their mass is extremely accurate and verified. A kit of weights from 1 to 500 grams has been used to analyze a wide range of sensors' output responses.

In particular, the weights used had masses of 10 gr, 20 gr, 50 gr, 100 gr, 200, gr and 500 gr.

Considering the sensing sphere of the FMA sensors, it seems a bit difficult to position weights directly on it because the contact area is too small and curved. So, it was necessary to develop a support system which has the following characteristics :

- the top support has to transmit the weight only on the contact sphere and not in anything other points of the system;
- it should have a support base to fit the PCB inside, leaving the sensor sensing area elevated;
- the top support needs to be bounded to the base but without contact to not transmit the weight to it.

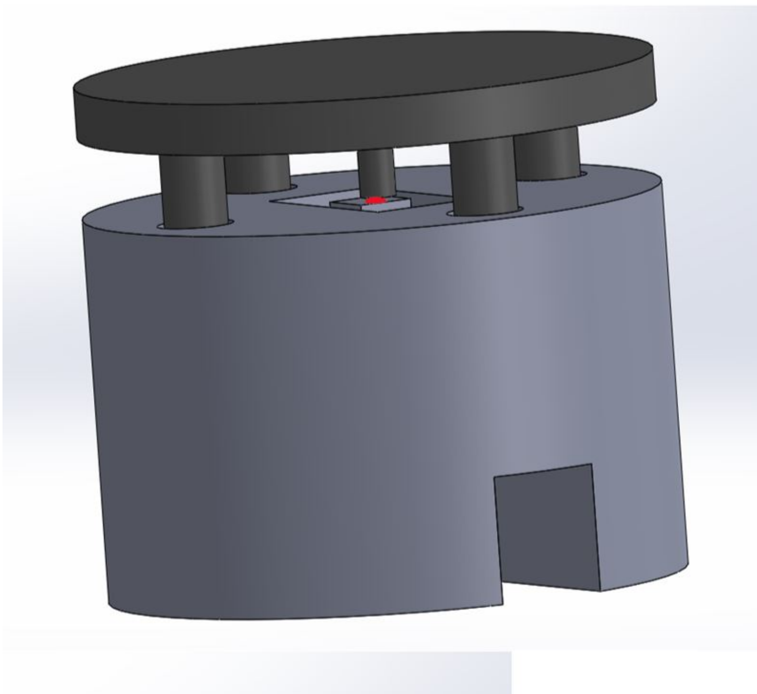

Figure 4.1: Assembly of the support system. In red is the sensing sphere of the sensor.

For the support base, a cylinder shape was chosen, with 45 mm as the diameter and a height of 30 mm. On the bottom area, two L-shape holes (visible in Figure 4.1 from the outside and in Figure 4.2 in section) are dug both to leave space for the wires connecting the headers under the PCB to the breadboard, and to eliminate material to print to streamline time and weight. On the top area, a rectangular hole for placing the PCB (16.25 mm x 9 mm) inside has been realised which connects on both sides to the L-holes. Additionally, four symmetric round holes have been realised on the top surface (6 mm diameter) to let the top support cylinder enter there for more stability.

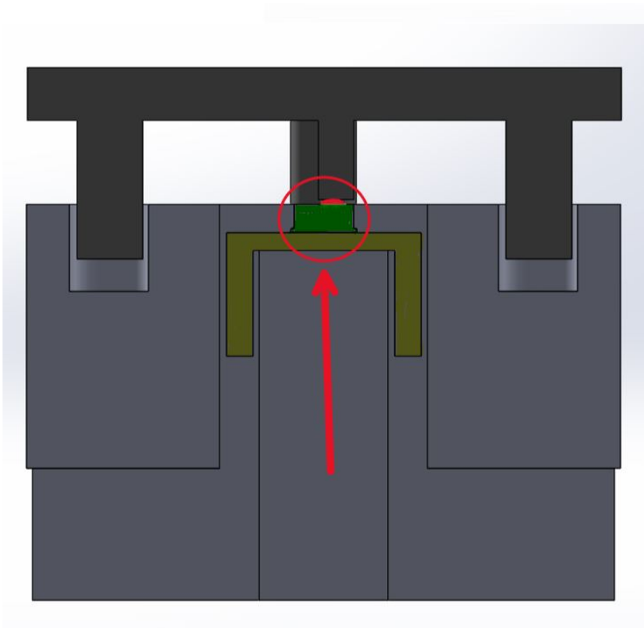

Figure 4.2: Section of assembly of the support system. Circled in red there is the sensor, with below the PCB on which it is soldered in yellow. The L-space for the wires under is also shown in this view.

For the top support, in fact, a circular base has been designed, always with a 45 mm diameter, and a thickness of 4mm. From there, four symmetric cylinders of 5 mm diameter and 10.5 mm height were extruded into a position aligned with the four holes of the bottom piece. Their diameter is lower than the holes in the base to not touch the boards. To have contact with the sensing element of the sensor, a smaller cylinder was extruded having 6 mm of height and 2.7 mm of diameter. Since the sphere is not centred on the sensor, this cylinder is 0.89 mm shifted from the centre of the system.

The design of both pieces of support has been performed on SOLID-WORKS. Once finished, the two parts of the support have been printed with the 3D printer Form3+ (figure (4.3)), which prints prototypical parts in economical industrial-grade resin (black or clear in this case) with optimal results using the Low Force Stereolithography (LFS) technology.

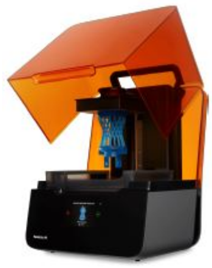

Figure 4.3: Form3 3D printer.

4.2 Experimental Setup

For analyzing the behaviour of the sensor when it is exposed to different loads on it, characterization measurement cycles have been done. In particular, the acquisition time has been set to 45 seconds and different kinds of measurements have been carried out:

- a cycle without any weights applied for detecting the baseline signal and the offset;
- different cycles with a constant weight on the top of the support just printed. The calibration weights used are gradually increased from 10 gr to 20 gr, 50 gr, 100 gr, 200 gr and at the end 500 gr;
- alternating loading and unloading cycles with different weights are performed to evaluate if the sensors are responsive to fast variations of force applied and if they restore their baseline in a quick way.

Both the 5N and the 15N force range sensors have been tested. All the measurements have been performed in the laboratories of the Department of Electronics and Communication (DET) in Politecnico di Torino (Figure

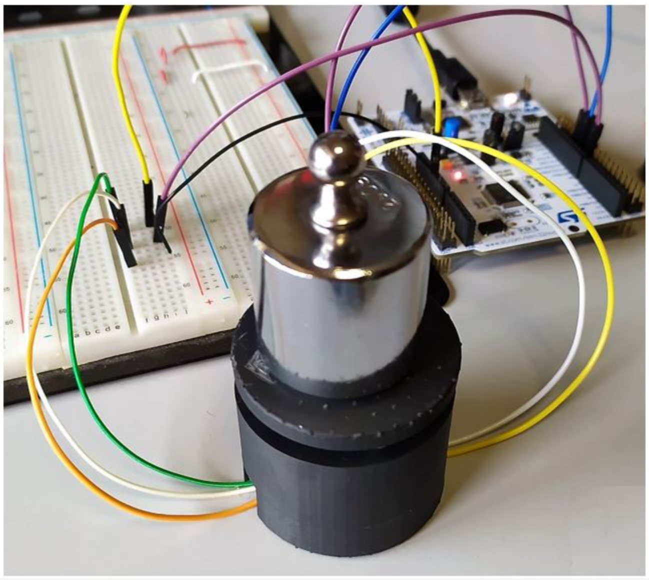

Figure 4.4: Configuration during acquisition.

4.4 and Figure 4.5). The acquisitions have been performed using the same firmware summarized with the flow chart in Figure 3.6.

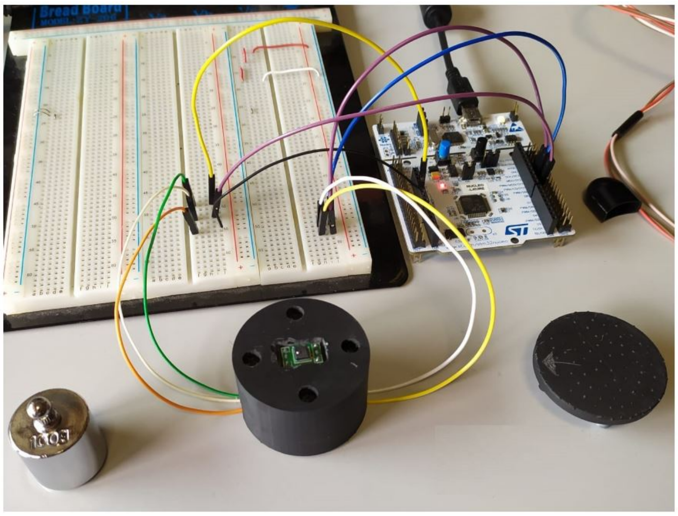

Figure 4.5: Separate components. It is possible to see the sensor on the PCB located inside the base.

4.3 Results and Graphs

After taking all the measurements and saving them on the laptop, the data have been processed and displayed using MATLAB software.

4.3.1 Baseline

The first measurements have been those related to the baseline. In fact, from them, it is immediately possible to notice if the sensor has good stability idle. In the table below, the mean values of the baseline output voltage of both sensors are shown along with their standard deviation.

Force Range (N)	Mean output (mV)	Standard Deviation (mV)
5	872.052	± 0.249
15	679.242	± 4.806

Table 4.1: Mean values of baseline and standard deviations for 5N and 15N sensor.

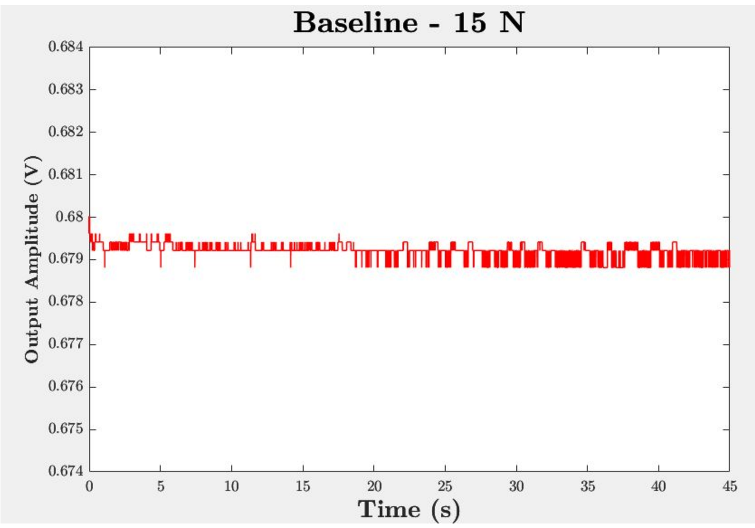

Figure 4.6: Voltage output with no weights on of the 15N force range sensor.

As it is possible to see, both sensors have a baseline value of a few hundred millivolts. Moreover, as demonstrated from the low standard deviation, the sensors maintain their output very consistently over time; specifically, the sensor with 5N as force range reaches the best stability, with an output variation of less than 0.1% of its mean value. The output recording of both sensors is shown in Figure 4.6 and Figure 4.7. As can be noticed, the signals provided by the sensor exhibit a nonlinear stepped pattern, corresponding to very small changes in the output. This suggests a very high sensitivity of the sensor to a sudden change in the force applied to it.

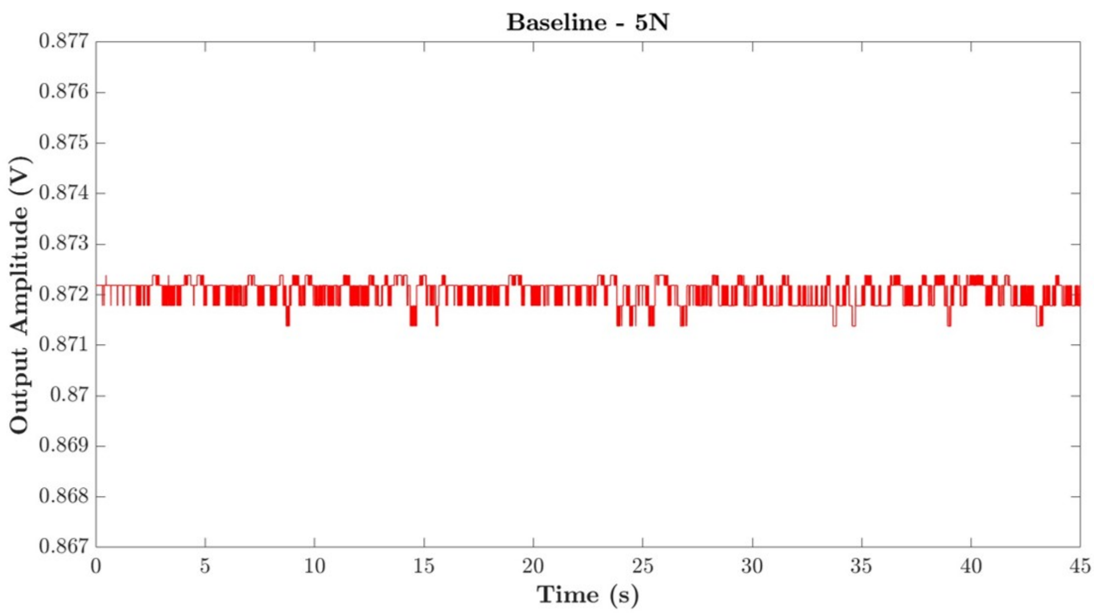

Figure 4.7: Voltage output with no weights on of the 5N force range sensor.

4.3.2 Constant weight - characterization curve

The tests have been performed by exposing the sensor to gradually increasing loads, as mentioned in the previous paragraph. Output values have been averaged over the measurement period; they are listed in Table 4.2 and Table4.3 below. As can be seen, the sensor with a 5N force range provides a larger output dynamic than the other one although at the same time it has a slightly higher standard deviation than the other sensor but is still very low.

Weight Mass (gr)	Mean output (V)	Standard Deviation (mV)
10	0.928	± 0.439
20	0.968	± 0.389
50	1.089	± 0.388
100	1.227	± 1.839
200	1.574	± 4.837
500	2.655	± 1.962

Table 4.2: Standard deviation and mean summarization table of the 5N sensor for each weight applied.

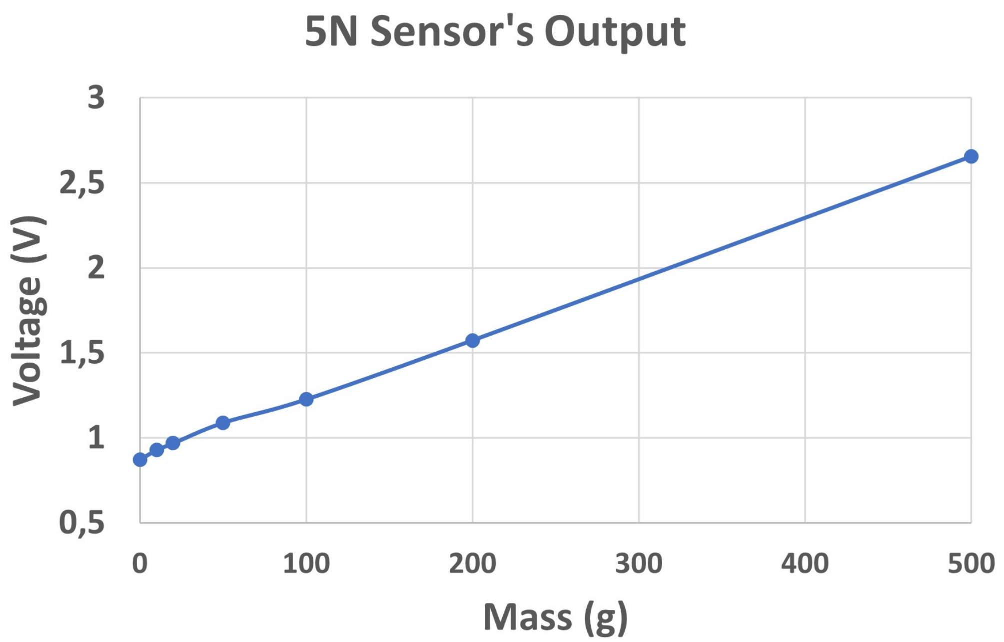

Figure 4.8: Characterization curve of the load cell with 5 N as force range.

Interpolating these data with a curve, the curve shows high linearity in all sections of both sensors' output, particularly in the area with low weights. This is very relevant for the thesis application because the displacement of the arteries produces a very low force, in the order of 1-2 Newton.

Weight Mass (gr)	Mean output (mV)	Standard Deviation (mV)
10	698.257	± 0.247
20	709.795	± 0.185
50	741.240	± 0.242
100	798.889	± 0.342
200	908.824	± 0.597
500	1241.147	± 1.257

Table 4.3: Summary table of the mean and standard deviation of the 15N sensor for each weight applied.

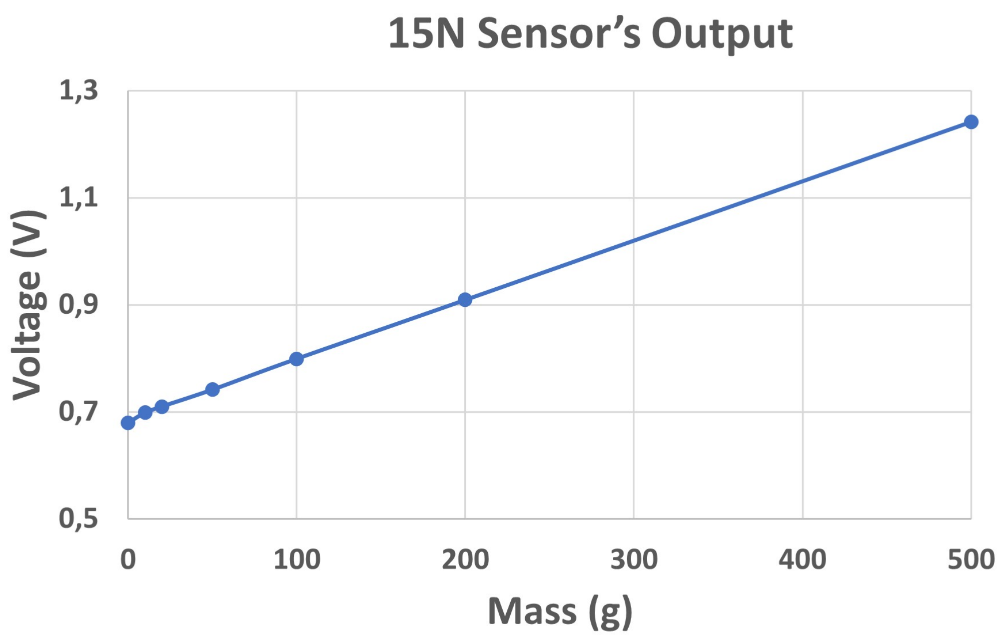

Figure 4.9: Characterization curve of the load cell with 15 N as force range.

4.3.3 Load/Unload cycles

For the load and unload cycles, some issues have come up. In fact, by increasing the weight used on the top support and repeatedly putting it on and taking it off, the system becomes a bit unstable. Most likely, this instability is due to the small contact area between the sensing sphere of the sensor and the central cylinder of the top support. Furthermore, the sensing element is not centred on the sensor, so the whole system loses symmetry. These factors reflect their influence on the measurements of both sensors used, particularly when higher weights have been used (100, 200, 500 gr): in fact, as can be noticed especially in Figure 4.10, the positioning of the weight on the support produces a drift in the output. For the lower weights, after about a second, the sensor restores a stable output and maintains it for the rest of the loading cycle. For higher weights instead, the sensors maintain the drift introduced by the load for almost all the loading time, causing measurements to be unstable, as shown in Figure 4.11.

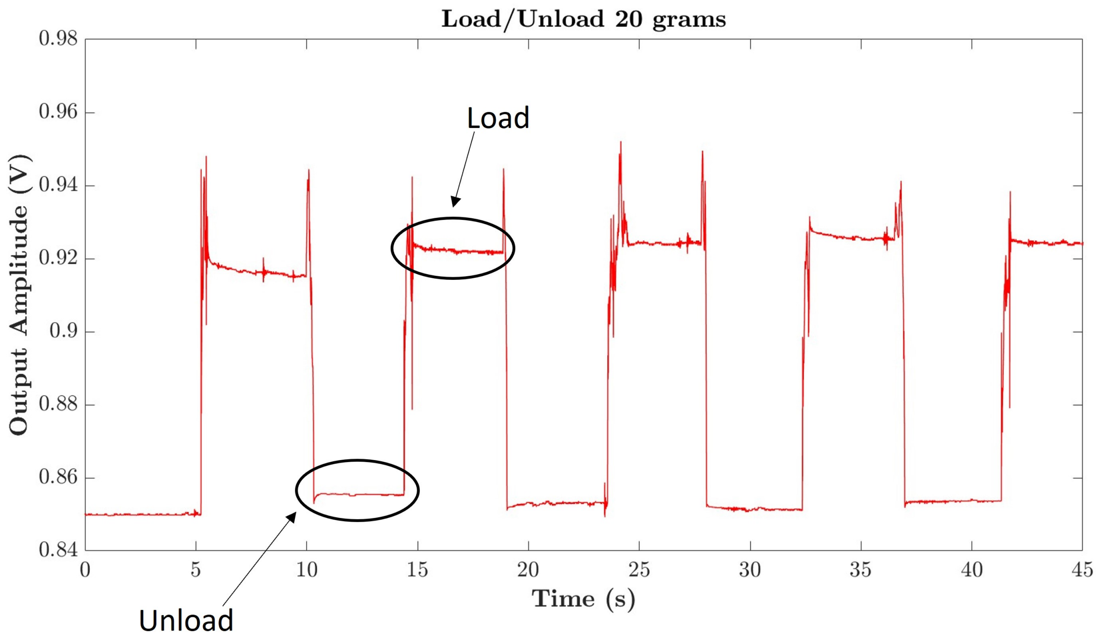

Figure 4.10: Load/Unload cycles with a weight of 20 grams (5 N sensor).

For these cycles of measurements, the 5 N proves to have a greater output amplitude and load sensibility. In fact, the rising edge when this sensor is under load is sharper than the other one.

Finally, comparing all the sensors' results, the 5N force range load cell offers a greater resolution, and a higher potential to detect smaller variations of force as in the case of detecting the pulse wave. Moreover, its stability both at no load and with a constant or alternating load applied to it is slightly higher than the other sensor.

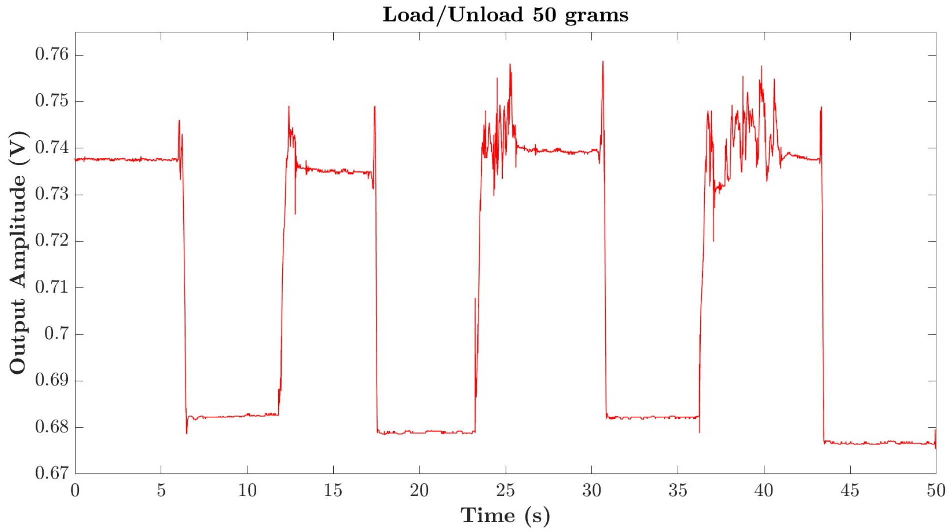

Figure 4.11: Load/Unload cycles with a weight of 50 grams (5 N sensor).

In particular the slope in the range between 0 and 20 grams has been considered to chose the better sensor:

$$Slope0 - 20 = \frac{(0.968 - 0.872)V}{0.020kg} = 4.8V/kg \tag{4.1}$$

$$Slope0 - 20 = \frac{(0.709 - 0.679)V}{0.020kg} = 1.5V/kg \tag{4.2}$$

The 5N force range sensor shows a greater slope in the range of force of interest for the application, which results in a grater sensibility and amplitude in the output. For these reasons, the choice of the sensor to use has fallen to the 5N force range one. So from this point onward, all measurements, reasoning, and discussions will only be about it and its performance.

Chapter 5

Integration with Bluetooth ATHOS system

In this chapter firstly a brief introduction to the Bluetooth Low Energy system is provided, with a nod to the microcontroller used for the Bluetooth implementation. After, a description of the components of the ATHOS Bluetooth prototypical system is given, along with the hardware changes made to it to make it suitable for the thesis project. In the end, a description of the firmware with Bluetooth data transmission is provided, with packet flow between the sensor and the laptop explained.

In Figure 5.3 the block diagram of the device is shown, with all the main components and their connections summarized.

5.1 Bluetooth Low Energy - Theory

Bluetooth Low Energy (BLE) is a wireless technology based on the standard BT 4.0+ for personal area networks to allow data exchange between devices in specified short-range frequencies. In particular, the operative frequency spectrum is on 2.4 - 2.4835 GHz, divided into 40 channels of 2 MHz width [39]. BLE, as its name suggests, is designed for low-power consumption applications like sensor data, control of devices, Internet of Things systems, etc. Operating in short-range applications and on the 2.4 GHz spectrum, obstacles like metal objects, human bodies, and water disturb its data exchange. On the other side, the short range and low power consumption reflect their positive effects on the low cost of chipsets and antennas for

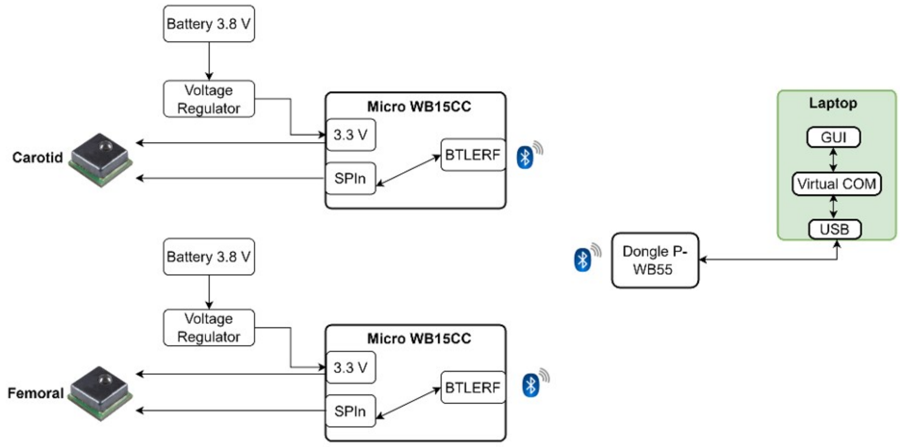

Figure 5.1: Block diagram with the connection between components in the device.

communication.

The BLE architecture is divided into three main layers: the *application, the host* and the *controller*, each of them composed of multiple sub-layers inside. The *controller layer* is the lowest layer of the architecture, it provides to establish the real connection between devices which can be clients or servers. In particular, the Link Layer manages the different states of the devices:

- *Advertising*: state in which the device sent out advertising packets to other devices to discover and read;
- *Scanning*: state in which a device scans for devices that are advertising;
- *Standby*: the device does not transmit or receive data;
- *Connected*: when two or more devices establish a link between them for exchange data.

The *application layer* handles data received from and sent to other devices. Practically, it is the code that the user writes for the BLE application.

The *host layer* is the most important one because it manages the control of several important aspects and protocols between clients and servers. By definition [39], a server is a device that exposes its data, sending responses, and notifications when requested, while a client interfaces with the server to read the server's data. It sends commands and requests, accepting notifications from a server. An important protocol contained in this layer is the Attribute Protocol (ATT): it defines how a server shows its data to the client and how they are structured. Data exposed by the server are organized in **attributes**, which are made up of a universal identifier (UUID); an attribute Handle, which is assigned by the server to uniquely identify a single attribute during the connection; the permission which indicates if the attribute can be written or read, notified or indicated, etc.; finally, there is the attribute value which is the real data to be exchanged. Many attributes that perform a specific functionality on the server form a *server*.

Above this protocol, there is the Generic Attribute Protocol (GATT) which defines the format of services and their characteristics as well as the methods used to interact with attributes, like service discovery, notifications, indications, etc.

5.1.1 Nucleo board STM32WB15CC

The Bluetooth® Low Energy (BLE) SIG specification v5.2 is complied with by the STM32WB15CC Nucleo-64 board, a Bluetooth® Low Energy (BLE) wireless and ultra-low-power device [37]. The microcontroller embedded in it [40] is based on the high-performance Arm® Cortex®-M4 32-bit RISC core operating at a frequency of up to 64 MHz; moreover, it contains a dedicated Arm® Cortex®-M0+ for performing all the real-time low layer operation. It also provides 320 Kbytes of Flash Memory, 48 Kbytes of SRAM, 7xDMA (Direct Memory Access) channels, 8 different timers, 1xSPI 32 Mbit/s, Inter-processor communication controller (IPCC) for communication with Bluetooth® Low Energy.

5.2 ATHOS System

A brief introduction to the ATHOS prototypical system has been provided in Chapter 2.4.2. In this section, the focus will be centred on the engineering part of the system, analyzing its components, the firmware that manages its functioning and the changes that have been made to the system to adapt it to the thesis aim. The probe is composed of a PCB inside on whose tip there is the sensor used [5]. The PCB and the sensor are alimented by a 3.7 V rechargeable Li-Po battery that is placed inside the holder just below the

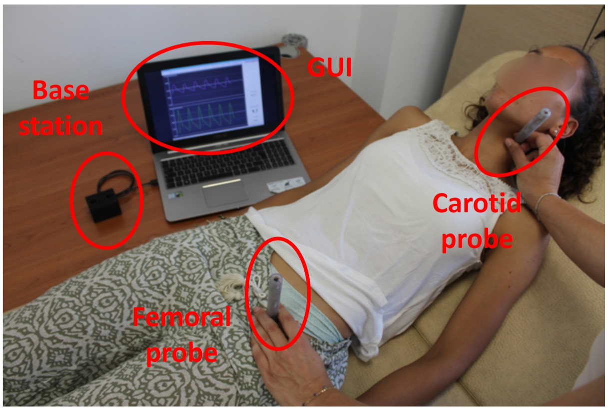

Figure 5.2: ATHOS system overview.

PCB. On the PCB, a switch is mounted and it is needed to turn ON and OFF the system. Moreover, on the bottom side, there are some magnets to facilitate the adhesion and stability of the pen in the charging base; also, there are some headers to bring some GPIOs on the base recharge station (specified in the section "Base Station" below).

Firstly, the Printed Board Circuits located inside the carotid and the femoral pen holders manage the sensors' readout. After that, the microcontrollers send data via Bluetooth to the Dongle, a receiver unit positioned in the Base recharge station provided by STMicroelectronics, which reorganizes data from both collecting sites before sending them to the laptop via USB. A Graphic User Interface (GUI) reads data arriving from USB on the Virtual COM Port and displays them in real-time on two different graphs.

5.2.1 PCB Pen

The Printed Board Circuit (PCB) manages many operations, from powering the sensor and the microcontroller mounted on it [40] to the implementation of a Radio-Frequency (RF) filtering stage for avoiding sample losses during data submission to the dongle.

First of all, an STLQ020C33R voltage regulator [41] is needed to transform the output voltage of the battery (3.7 V) into 3.3 V which is the power supply of both the microcontroller and the sensor. A mechanical switch is positioned on the top of the PCB; when it is turned on, its output is connected to the output of the voltage regulator, so the system starts to be

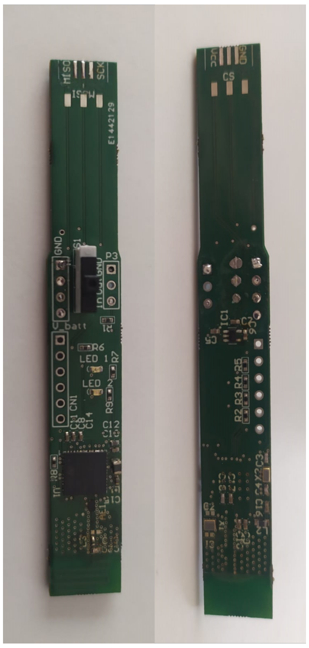

Figure 5.3: Photo of the PCB (front-back).

supplied. A green and a red LED are positioned just below the switch and when the system is powered they toggle one time. If this happens, it means that the system is working properly.

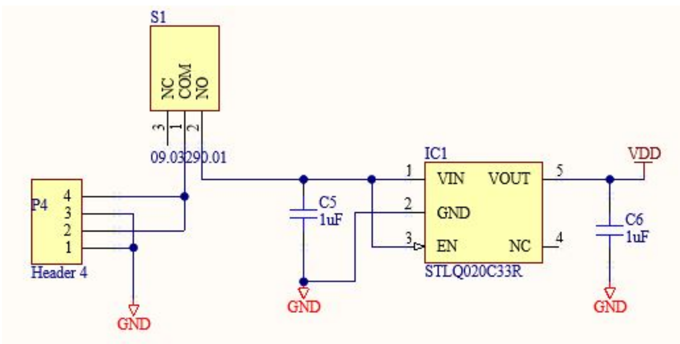

Figure 5.4: Schematic of the voltage reference system.

On the front side of the PCB, the microcontroller is soldered. Its pins are connected with the same resistance, capacitors and inducers that are mounted on the correspondent Nucleo-board. Of particular relevance are the two oscillator crystals (32 MHz and 32 kHz frequencies). They are soldered on the back of the PCB and their output is used to obtain the clock frequencies of the system. To perform their important function, they must be soldered in a specific direction otherwise the system does not work.

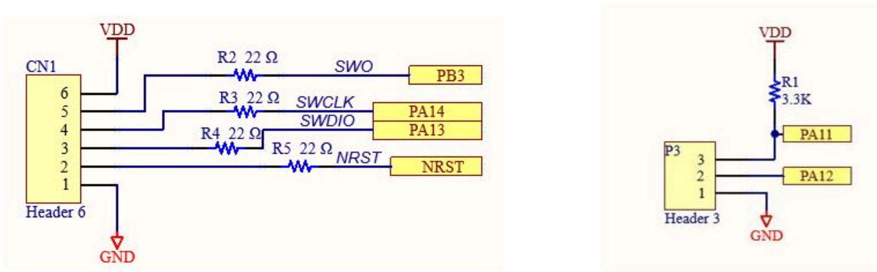

Figure 5.5: Schematic of the headers responsible for the firmware upload (on the left) and the synchronization (on the right).

On the front side of the PCB, there are also two main groups of headers. Particularly, the first one is composed of six headers which allow interfacing with the microcontroller for the upload of the BLE stack architecture (using STM32CubeProgrammer). Moreover, it is possible to upload the firmware for the sensor readout connecting these headers to a Nucleo-board with the ST-Link.

The *CN1*, instead, is made up of three headers which are connected to the microcontroller GPIOs responsible for the synchronization of the system. More in detail, these headers are connected to the spring connector of the base station where they establish a connection with the respective GPIOs of the other probe (better explained in Chapter 5.2.3.

Last but not least, a radio-frequency system is implemented on the bottom part of the PCB. It is composed of a meander 2.4 GHz antenna for PCB which transmits data acquired from the microcontroller to the dongle, a 2.4 GHz low-pass filter chip matched for the STM32WB components and an antenna matching network made up of two capacitors and one inductor. This system provides the data transmission to the dongle as said before while selecting the band to avoid noises around which can interfere with the transmission causing losses or delays.

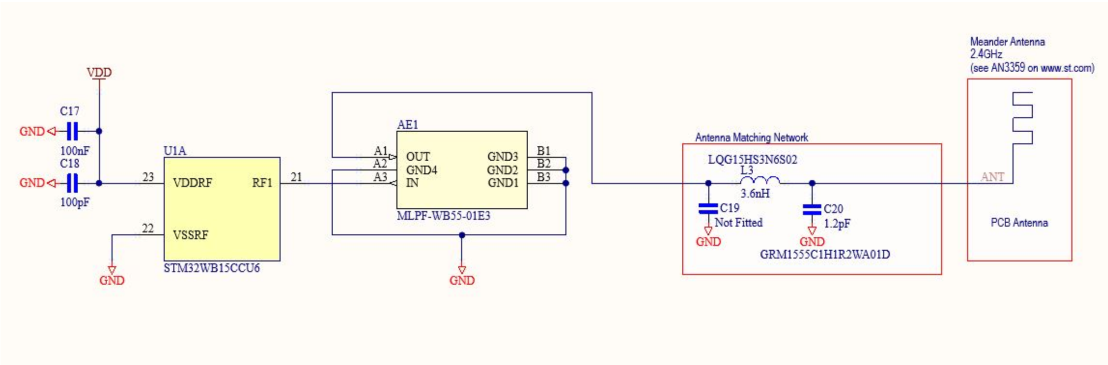

Figure 5.6: Schematic of the RF hardware.

5.2.2 Round adapter

A round PCB adapter has been printed because the rectangular PCB used for characterization is not suitable for the application; moreover, the pads below the sensor do not correspond to the tracks on the main PCB of ATHOS. It has been designed using Altium, with a diameter of 10 mm and a thickness of 1 mm. The sensor is placed on top of it and protrudes slightly from the probe.

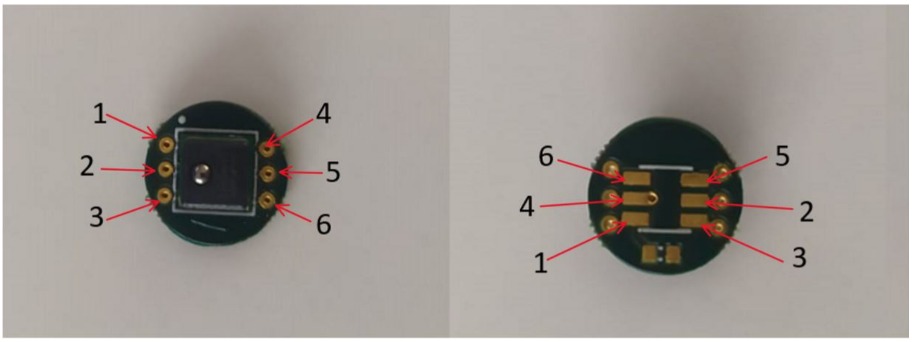

Figure 5.7: Round adapter. View of the top side (left) and bottom side (right). Legend of the pads: 1 = V_{cc}, 2 = NC (no contact), 3 = SCLK, 4 = CS, 5 = MISO, 6 = GND.

5.2.3 Base Station

The base station is composed of a base support in which is placed a PCB necessary to perform the recharge of batteries while connected and the connection of the two probes. The dongle is wired to this PCB and using a USB-USB adaptor the base station can be connected to the laptop. A case is put on the base to cover all the hardware components and to have two holes in which insert the probes. The probes can be inserted in the base station easily following a guiding groove in the case and, when they are in, they are connected to the base station and between them thanks to spring connectors positioned on the base. Additionally, to hold the probes firmly on the base, a set of magnets is placed around each spring connector to attract the magnets placed in the pen holder.

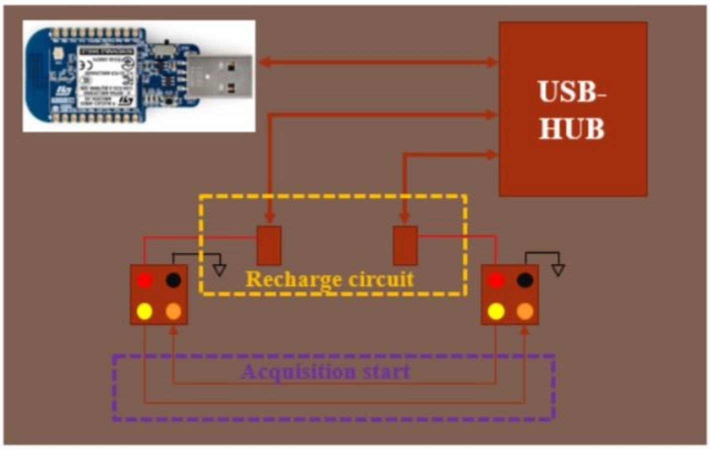

Figure 5.8: Schematic behaviour of the base station: the USB-HUB receives data from the dongle and recharges the batteries of the pen.

The base station acts as batteries recharge and Bluetooth synchronization, as shown in Figure 5.8, thanks to the creation of connections between two GPIOs (General Purpose Input/Output) pins of both probes. When one of the two probes is removed from the base, this connection is broken and the GPIOs have a transition from the low logic level (they are shorted when connected to the base) to the V_{DD} via a pull-up resistor (3.3 kOhms nominals), as shown in Figure 5.9. When this transition is detected by the firmware, the timer that temporizes data acquisition from the sensors is started, so the acquisition starts. This aspect is discussed more in detail in Paragraph 5.3.

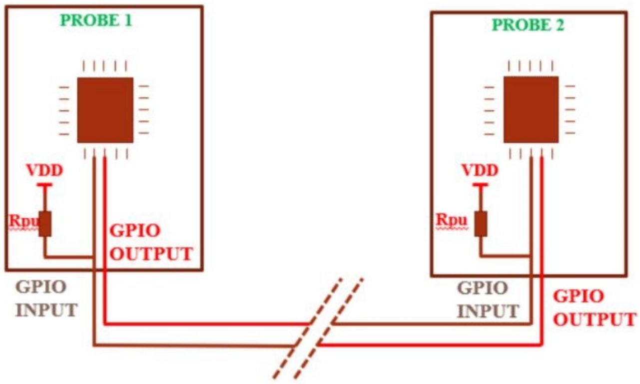

Figure 5.9: Synchronization setup: when the connection between the two pins is broken, the system starts to acquire data from sensors.

5.2.4 Support adjustments

The carotid and femoral pen holders differ from each other just for the tip: the femoral one has a larger area on the tip because is more suitable for the collecting sites, while the carotid holder is smaller on the top for fitting better on the carotid site. They have a length of 14.3 cm, a bottom diameter of 1.63 cm and a top diameter of 1.83 cm for the femoral one and 1.53 for the carotid one. All the edges and corners of the support are blunted for better handling.

The pen holders used in ATHOS have been tweaked to make some improvements to the efficiency and aesthetics of the system. Firstly, the locking system has been redesigned. In the previous version, the holders were composed of two units which present few guides for closing it: fundamentally, they were two different types of guides, one per side of the holder, which fit perfectly inside each other. As time passed on, they tended to widen, opening slightly the holders. Additionally, they were a little bit difficult and hard to close.

For that, a new latch system has been implemented, increasing the number of latch rails and spacing them equally apart. The guides slide between them until they snap and indent each other.

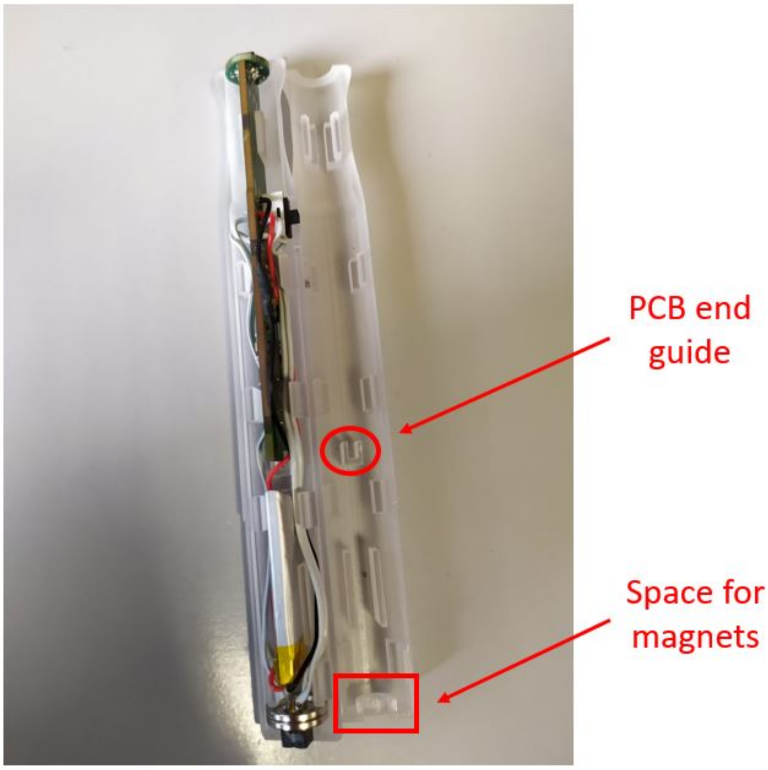

Figure 5.10: View of the inside of the pen holder with the new changes. It is possible to notice the multiple guides that allow the closure, with the two added parts in red.

On the intern side of the probe, end support for the PCB has been added to keep the PCB from sliding up and down inside, keeping it more stable (Figure 5.10). Moreover, on the bottom side, a new cavity has been realised where the magnets can fit in.

5.3 Firmware Bluetooth implementation

With the integration of the sensor in the ATHOS BLE system, the firmware for the sensor readout has been modified, adapting it to the Bluetooth transmission of data.

Data Readout

Implementing the Bluetooth architecture, data buffering had to be performed. From each sensor, a circular buffer with a payload of 16 bytes is set. The first 14 bytes are reserved for sensor measurements: considering that each readout is 2 bytes long, for each collecting site 7 samples are acquired before sending the data. The last two bytes are left for the ID of the board, needed in the next steps to understand from which collecting site the data come, and for a counter which represents the number of buffers already sent.

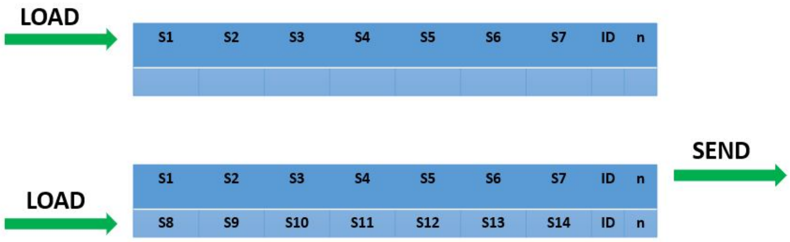

Figure 5.11: Concept of a circular buffer (S=sample, ID=identification of the board, n=number of packets already sent).

As said a few lines above, a circular buffer was implemented for each probe: it is a two-line buffer in which alternatively a line is set to store the data read and after is set to send the buffer to the dongle receiver, as can be noticed in Figure 5.11.

The sampling frequency of the system has been changed: using 400 Hz sending data to the dongle with this buffer payload caused data losses during Bluetooth transmission. So, it has been decreased to 200 Hz maintaining the same buffer structure. With this system, the time elapsing between two different buffers arriving at the laptop is equal to:

$$refreshtime = \frac{1 * 14byte}{200Hz} = 70ms \tag{5.1}$$

which is a good trade between the payload limit imposed by the BLE architecture and the refresh time of the COM port in the laptop which is at least of about 50 ms.

Dongle

The dongle receiver performs a crucial role in the whole system. In fact, firstly it receives one different buffer from each probe and saves the first 15 bytes of each received buffer one consecutively to the other in a 30-bytes buffer. After that, it makes a check on the bytes where the ID boards are located: whether a buffer has arrived from both probes, so it performs the reorganization of data. An implemented function performs the unpacking of the buffer, taking one sample from each probe and alternating them one by one. As a result, a 28-byte buffer is ready to be sent to the GUI via USB.

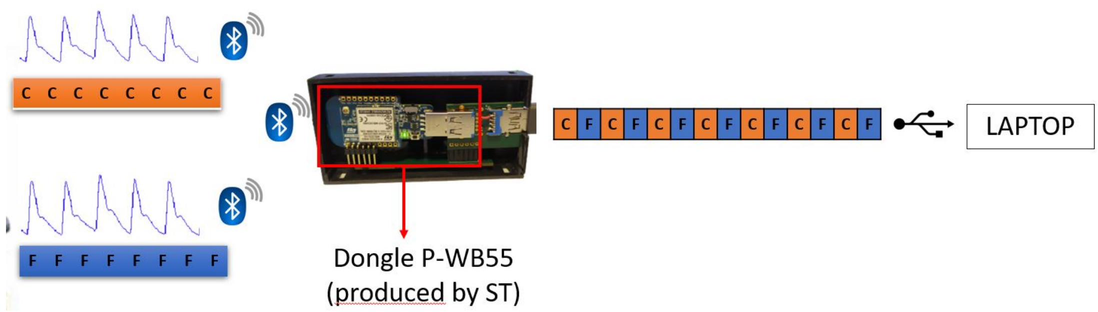

Figure 5.12: Schematic of the reorganization occurring in the dongle (C=carotid sample, F=femoral sample).

Synchronization

As mentioned in Chapter 5.2.3, the acquisition from the two sensors is synchronized to let the system start at the same time for the following evaluation of the PWV and PTT. The two probes are positioned in the base station where two of their GPIOs are connected and short-circuited among themselves. An internal timer of the microcontroller is set to start sensor readouts and its activation is triggered by the removal of one of the probes from the base station. The timer activation generates a command which is sent to the GUI via USB to let the GUI ready to read the sensors data from a Virtual COM Port and display them in real-time in two different graphs.

5.4 Graphic User Interface

The Graphic User Interface used in the ATHOS system has been developed in Visual Studio. This GUI has been adapted to the thesis application by bringing some changes. It reads data from the Virtual COM Port of the laptop which arrive from the dongle. The GUI read the data buffer and plots each sample read in real-time in two different graphs, one for the carotid and one below for the femoral signal. In parallel, the data are saved in a binary file for post-processing on MATLAB, which will be discussed in Chapter 6, to extract the PWV value.

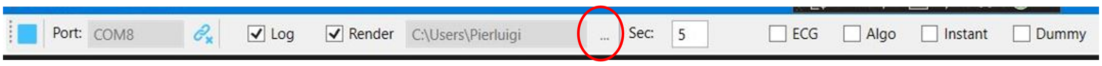

Figure 5.13: Detail of the command bar of the GUI.

The command bar with the main commands of the GUI is situated above the graphs. It is composed of several buttons and labels with different functionalities:

- the Play/Stop button is the first command. It has to be pressed to start or stop data plotting;
- the paperclip button is the button for connecting the laptop to the COM port where the base station with the dongle is connected. When the connection is established, the name of the port is visualized on the label on the left of the button;
- circled in red in Figure 5.13, the button with three points needs to be pressed to indicate a directory where to save the file generated; the chosen directory is shown on the label at its left. At this point, to correctly save the file, it is necessary to check the check box named "Log";
- the text box named "Sec" gives the possibility to indicate how many seconds have to be displayed in each chart;
- the check box "Algo", if it is checked, implements an algorithm to automatically generate a report of the PWV and the other parameters;

- the check box "Instant", if it is checked, displays the instant value of PWV;
- the check box "Dummy" has to be checked to visualize the dummy signal which is a signal used for debugging the system and checking if it is working properly.

To make the system work properly, the interface should be started when both the pen holder are on and positioned in the base station. When one of them is extracted from the base station, the system sends a command to the GUI which recognizes it and starts to display samples in both graphs.

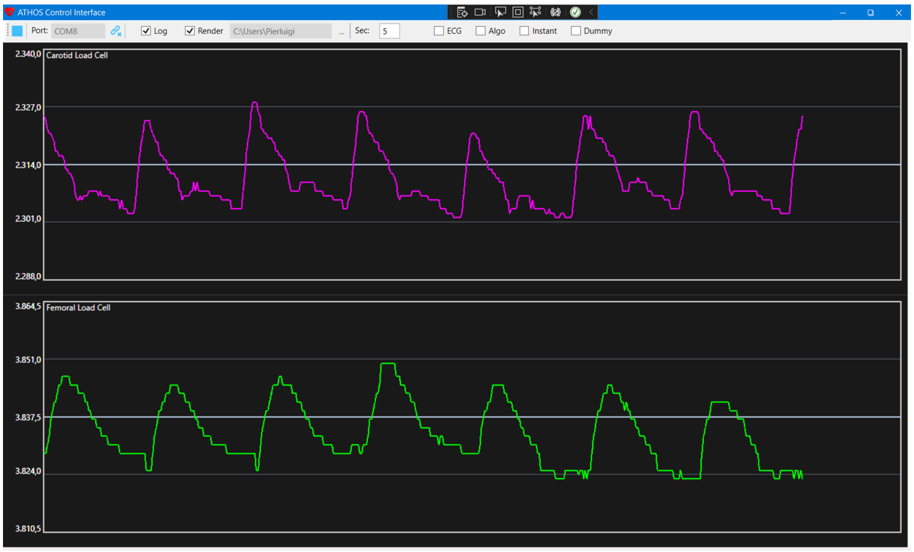

Figure 5.14: Graphic layout of the GUI.

Chapter 6

Data Acquisition and Statistical Analysis

This section first provides an overview of the first signals acquired with sensors and after a brief description of the algorithm implemented to extract the PWV value. After describing the protocol followed in "A.O.U. Città della Salute e della Scienza" in Turin, the results of the clinical tests performed there are displayed.

6.1 Preliminary Analysis

Figure 6.1: Final system: ATHOS probes on the base station with load cells soldered on the tip of them.

The first measurements have been made using the system described in Chapter 5.2. These acquisitions have been carried out to test the behaviour of the sensors during the application on human skin. The last ten seconds of each measurement have been taken into account, discarding the last two overall as they coincided with the removal of the probes from the collection sites.

An unexpected issue emerged during the visualisation and analysis of the raw signal acquired by the sensor. Although in the characterisation phase the sensor's behaviour seemed to be linear, the signals recorded when measuring the pulse wave from both collecting sites have shown a quantization in the signal, a stepped pattern (as shown in Figure 6.2) which can be comparable with the background noise observed during the characterization in Figure 4.7.

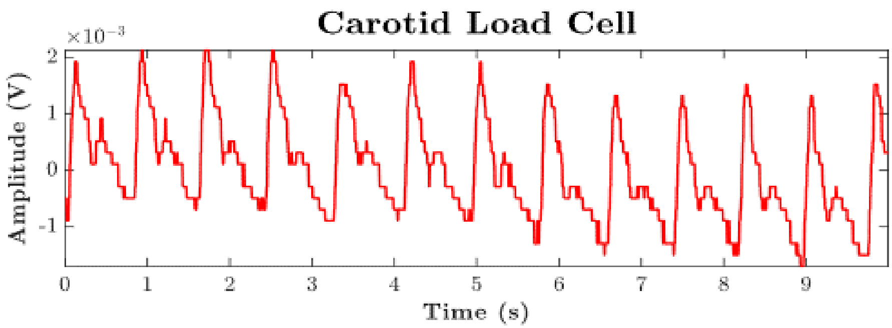

Figure 6.2: Ten seconds of the raw carotid pulse wave acquired. The poor resolution of the signal is clearly visible.

This behaviour resulted in poor signal resolution, most likely due to a hardware limitation of the sensor. Being a digital sensor, it has not been possible to design a conditioning circuit to stabilise the sensor output. Furthermore, as no more accurate information on its construction was provided by the manufacturer, it has not been possible to investigate what might have caused this behaviour.

Using the filtering stage implemented in the ITP algorithm (explained in detail in Chapter 6.2), the signal has not shown anymore a poor resolution as expected (Figure 6.3), but post-processing filtering only masked an intrinsic limitation of the sensor. This limitation has been reflected in the results, probably worsening the performance of the system.

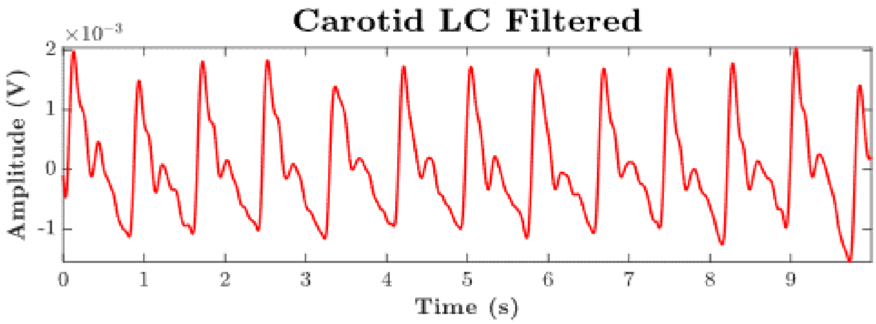

Figure 6.3: Ten seconds of the carotid pulse wave filtered in MATLAB.

6.2 Intersecting Tangent Point Algorithm

The intersecting tangent point method has been demonstrated [42] to be the most reliable method for PWV estimation. In fact, it permits the extrapolation of the signal "foot" of the pulse wave, defined as the point on the signal where a horizontal line intersects the tangent to the point of maximum first derivate and a line passing through the minimum before the beginning of the systolic peak, according to the projection on the signal.

The following steps have to be implemented to perform the algorithm:

1. firstly, a band-pass filter of the 4^{th} order has been implemented, with cut-off frequencies of 0.5 Hz and 10 Hz, to remove the DC-offset component of the signal, the high-frequency noise and the network interference (at 50 Hz);

2. a 4^{th} order low pass filter with a cutoff frequency of 2 Hz is applied. The signal becomes a sinusoidal and its relative minimums are considered as the *n event starters* of the blood pulse to identify the number of blood pulse's initial event. The cardiac cycle (T) is consequently defined as the number of samples between two consecutive event starters;

3. a *±T/3* signal window is selected from each event starter. In this window, all the minimums are detected. A threshold of 50% of the lowest minimum y-coordinate detected is defined; if the y-coordinate of a minimum is lower than the threshold, this minimum is saved;

4. every blood pulse must be taken into account separately before moving

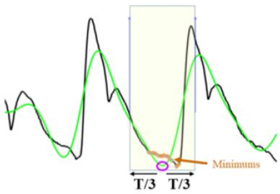

Figure 6.4: Extraction of the minimum point in ITP algorithm [4].

further with the "foot" extraction. For this, starting with each event initiator, a window of T samples must be assessed individually;

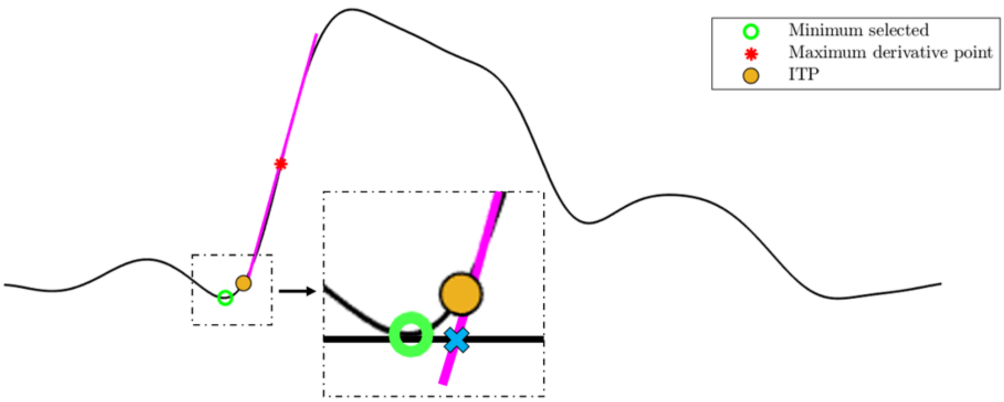

Figure 6.5: Intersecting tangent point detection [4].

5. the intersecting tangent point method is performed in the T-window. First, the signal's first derivate is calculated. The first maximum of the first derivate is then found from each minimum retrieved in step 3; the closest minimum to the maximum edge slope is then picked. After, both the horizontal line through the minimum and the tangent passing through the maximum of the first derivate are traced. Their intersection is projected on the signal to obtain the "foot" of the pulse-rising edge;

6. the PTT value is assessed if the detection of the foot is achieved through both the carotid and femoral pulse waves and if the foot of the carotid pulse is antecedent to the respective foot of the femoral pulse, otherwise the foot is discarded (Figure 6.6):

$$PTT = foot_{fem} - foot_{car} \tag{6.1}$$

The value of PWV is calculated as the ratio of the distance carotid-femoral (displayed in Table 6.1) and the PTT just assessed;

7. the algorithm restarts from step 5, considering a new window of T samples.

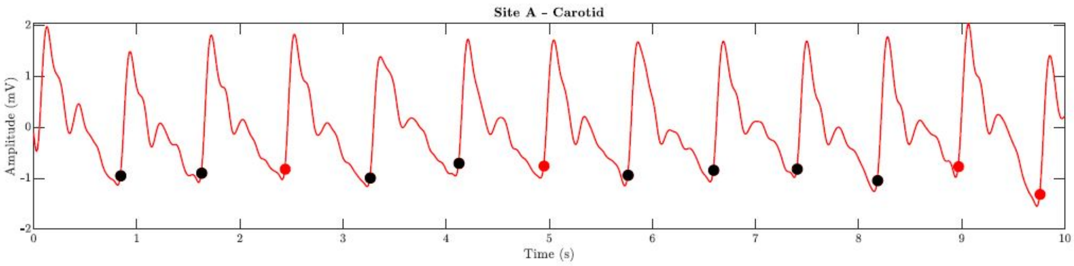

Figure 6.6: Pulse signal with the foot of the wave identified. In red are displayed the foot discarded, in black the holed ones.

6.3 Experimental protocol

Five subjects have been tested with the device developed in the thesis. The ATHOS system had authorisation from the Bioethics Committee, so also the thesis system has it. The medical operators perform the measurements with the two devices by alternating among them for every subject. For each subject, this experimental protocol has been followed:

- physiological parameters about the patients have been taken (showed in Table 6.1;
- blood pressure is measured with a sphygmomanometer;
- after selecting the optimal collecting site on the carotid and the femoral artery, the direct distance between them is measured with a meter;
- three measurements with SphygmoCor and the load cell are performed. Each acquisition has a duration of 30 seconds per device.

Subject	Age	Gender	Weight (kg)	Distance(mm)	BP(Dya-Sys)
1	26	F	54	448	103-73
2	24	M	72	516	117-76
3	26	F	59	480	128-77
4	26	M	80	496	118-83
5	24	M	72	496	120-72

Table 6.1: Physiological parameters of the five subjects (BP=Blood Pressure; M=male, F=female).

Figure 6.7: PWV signals acquisition. It is possible to see the simultaneous acquisition both from the carotid and the femoral site.

6.4 Results and Statistical Analysis

The ITP algorithm is performed on MATLAB and, as a result, it provides a report where the values of PWVs, standard deviation and the pulse waves collected in the carotid and femoral site are shown. The mean values of PWV of the three several acquisitions have been averaged for each subject, both on SphygmoCor and the thesis' system.

As it is possible to notice in Table 6.2, the values of PWV estimated with the BLE system are generally lower than the SphygmoCor ones. Moreover, they show a higher standard deviation which results in greater variability of the output, in particular subjects 1 and 5.

Subject	PWV SphygmoCor	SD	SD%	PWV Load cell	SD	SD%
1	5.9	0.33	5.6	4.63	0.67	14.4
2	5.87	0.27	4.6	4.57	0.33	7.2
3	6.8	0.37	5.4	5.93	0.33	5.6
4	6.27	0.4	6.4	5.55	0.45	8.1
5	6.5	0.4	6.1	6.5	0.8	12.3

Table 6.2: Comparison between PWV mean values obtained (in m/s) with the two different system (*SD=Standard Deviation*, SD%=Standard Deviation in percentage).

It can be noted from Figure 6.8 that for subject number 5 the PWV value is the same with a higher standard deviation, while for subjects 1 and 2 the PWV values obtained are slightly more than 1 m/s lower than the PWVs obtained with SphygmoCor, as can be seen in Figure 6.10. Also subjects 3 and 4 show a lower value of PWV when tested with the thesis' system.

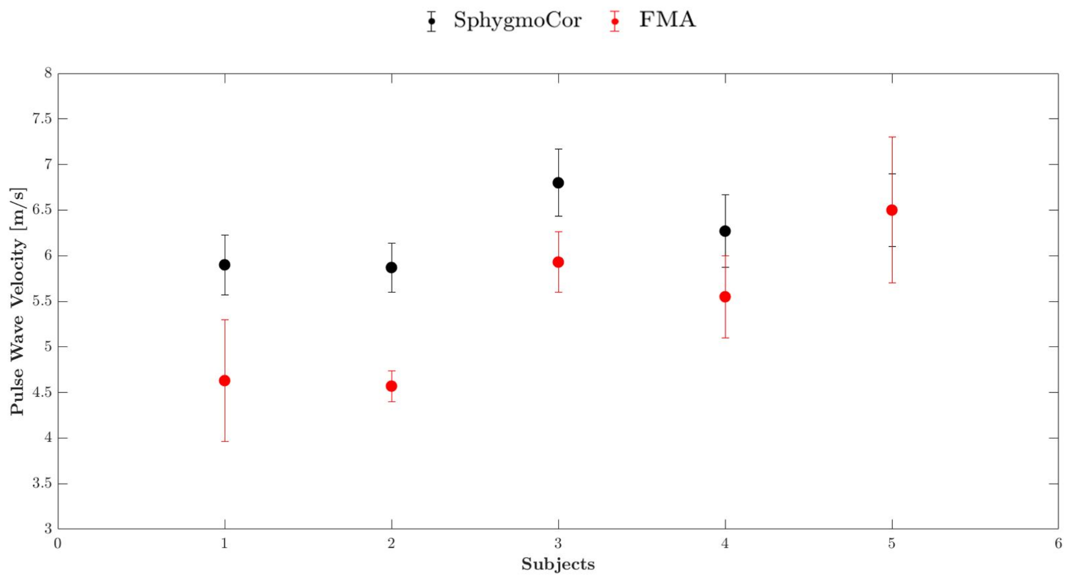

Figure 6.8: PWVs values obtained for all the 5 subjects. The standard deviations are displayed in the error bars. Each value of PWV is the mean of the three tests performed.

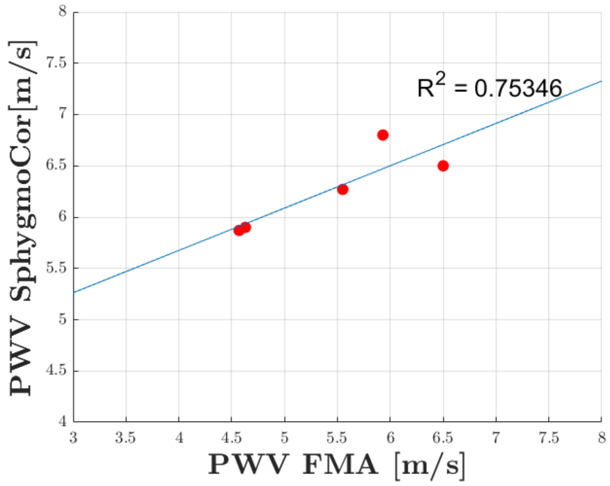

Figure 6.9: PWV measurements with the system developed in this thesis vs SphygmoCor: the scatter plot shows a linear correlation between the measurements made by the two instruments across all subjects.

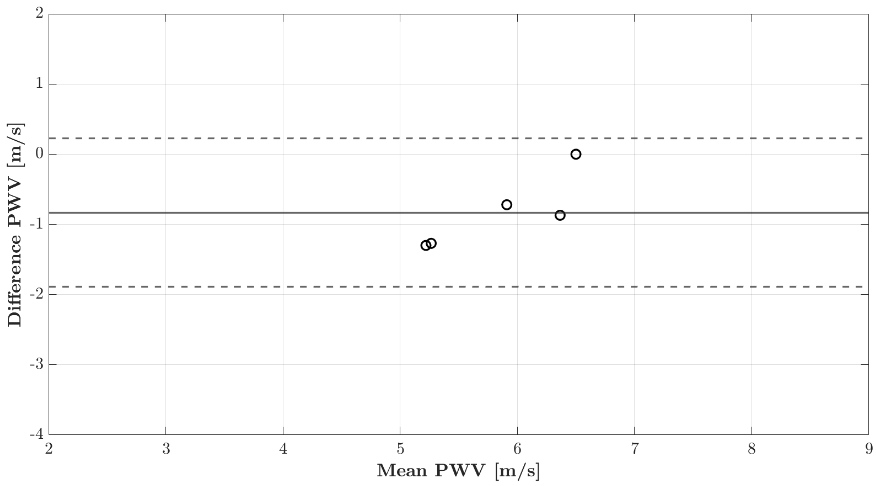

Figure 6.10: Bland-Altman plot between the performances given by Sphygmocor and the thesis device.

As can be seen from Figure 6.9, the *determination coefficient* R^2, which is the square of the correlation coefficient R, is 0.75346, indicating a linear correlation between the measurements of the two devices. The linear regression line plotted in blue shows that the correlation between the measurements is not optimal but still quite good, except for a little discrepancy on one subject at the top of the graph.

Figure 6.10 shows the Bland-Altman plot which represents the agreement distribution between the two devices [43]. The graph is composed of three lines: the continuous one represents the mean difference between the PWVs value of the two devices ($\bar{u}$) which is -0.8 $\pm$ 0.5285 m/s. The dotted lines are traced in correspondence of $\bar{u} \pm 2s$, where s is the correspondent standard deviation. It can be noticed that all the subjects are within the range of values bounding the graph, so it can be asserted that there is no bias in the data, despite the mean difference between the PWVs estimation of the two devices is slightly high. Furthermore, the sample on which is performed the analysis is small, so a more significant population have to be validated with this device to confirm or refuse the results obtained.

Chapter 7

Conclusions and future works

The aim of this thesis was to develop a low-cost and non-invasive system for Pulse Wave Velocity (PWV) estimation using load cells or force sensors. This parameter represents the speed at which the pulse wave in arteries propagates and it has been demonstrated that it is clinically significant for diagnosing and preventing cardiovascular diseases. The system developed during this thesis work has to be based on a sensor that can replace the tonometers used in the ATHOS prototypical system developed by the MiNES research group at the Politecnico di Torino, as they are prototypical and not freely available on the market. Micro force load cells produced by Honeywell are chosen in pursuit of this goal because of their small dimensions, low force range and low purchase costs.

The first part of the thesis work has been focused on performing a correct sensor readout and characterizing its response when exposed to different types of loads on it. After the work of sensors characterization, it has been noticed that the sensor shows high stability when exposed to a static load, while at the same time a high sensibility even if exposed to small variations of force as in the case of arteries displacements.

Then, the sensor has been integrated into the ATHOS prototypical system replacing the tonometers and making some adjustments to the setup for checking his performance. The system has been tested in "A.O.U. Città della Salute e della Scienza" in Turin to compare its performance with the SphygmoCor, the golden standard in clinics for PWV estimation. The results obtained show that the system based on the load cell generally underestimates the value of PWV compared to Sphygmocor, showing also a high instability of the performance due to a slightly higher standard deviation than the one resulting from the gold standard.

This behaviour could come from the stepped pattern that the sensor output shows, introducing signal distortion and altering the results. The poor resolution of the sensor shown in the signals acquired in human skin can reflect an hardware intrinsic limitation which may have worsened the performance of the system. In the future, reduced signal distortion and a more efficient computing implementation could be achieved by applying a real-time bi-quadratic filter on digital signals. Nevertheless, the system with such sensors results to be user-friendly for healthcare professionals. An important aspect is the positioning of the sensing sphere: the acquired signals show an improvement in their quality the more the sphere is placed precisely on the collecting site. The sensor shows a stepped pattern, suggesting a limit in its resolution. For this reason, in the future, a possibility to improve its performance could be an array of these sensors, positioning four of them to form a square and obtaining an array of 2x2 dimensions.

The population sample on which has been tested the thesis' system is too low to certify the sensor's behaviour. To overcome this problem, much more subjects are needed to validate the system's performance and to have a more reliable and robust evaluation.

An improvement that can be made in the future is to optimise the Bluetooth transmission to find a higher sampling frequency. For the thesis work, it has been reduced from 400 to 200 Hz to allow the transmission of all acquired samples without loss of information. A new trade-off can be found by increasing step-by-step both the sampling frequency and the buffer dimension, which for lack of time it was not possible to carry out in more detail. The lower sampling frequency could also impact the visualization of the pulse wave, emphasising the sensor stepped pattern.

If these future steps will not lead to a significant improvement in the performances and in the quality of signals, a new load cell should be found in the market, comparable in dimensions to the one analyzed in the thesis work. In fact, despite their behaviour and performances, this thesis work has proved that load cells could be used to measure the PWV, opening the possibility on the research of a new type of sensor for this application.

Bibliography

[1] World Health Organization. *Cardiovascular diseases (CVDs)*. 2021. URL: `https://www.who.int/news-room/fact-sheets/detail/cardiovascular-diseases-(cvds)` (cit. on p. 1).

[2] G. A. Roth, G. A. Mensah, V. Fuster, et al. «Global Burden of Cardiovascular Diseases and Risk Factors, 1990–2019: Update From the GBD 2019 Study». In: *Journal of the American College of Cardiology (JACC)* 76.25 (2020), pp. 2982–3021 (cit. on p. 1).

[3] S. Bernick and C. Davis. *The economic cost of cardiovascular disease from 2014-2020 in six European economies*. Tech. rep. Center for Economic and Business Research (CEBR), Aug. 2014-2020 (cit. on p. 2).

[4] Buraioli I., Lena D., Sanginario A., Leone D., Mingrone G., Milan A., and Demarchi D. «A New Noninvasive System for Clinical Pulse Wave Velocity Assessment: The Athos Device». In: *IEEE Transactions on Biomedical Circuits and Systems* 15.1 (Feb. 2021), pp. 133–142. DOI: `https://dx.doi.org/10.1109/TBCAS.2021.3058010` (cit. on pp. 2, 19, 22, 25, 68).

[5] Buraioli I., Valerio A., Sanginario A., Leone D., Mingrone G., Milan A., and Demarchi D. «Live Demonstration: Wireless Device for Clinical Pulse Wave Velocity Evaluations». In: *IEEE BiOCAS*. 2022 (cit. on pp. 2, 25, 26, 53).

[6] ST. *LPS22HB - MEMS nano pressure sensor: 260-1260 hPa absolute digital output barometer*. URL: `https://www.st.com/en/mems-and-sensors/lps22hb.html` (cit. on pp. 2, 25).

[7] V. C. Scanlon and T. Sanders. *Essential of Anatomy and Physiology*. Fifth. Philadelphia, USA: F. A. Davis Company, 2007 (cit. on pp. 4, 7, 9, 11, 14).

[8] C. L. Stanfield. *Principles of Human Physiology*. Pearson, Benjamin Cummings, 2011 (cit. on pp. 4, 7).

[9] J. Gordon Betts, Kelly A. Young, et al. *Anatomy and Physiology*. Open Stax, 2013 (cit. on pp. 5–7, 12, 13).

[10] I. Peate and M. Nair. *Fundamental of Anatomy and Physiology for nursing and healtcare students*. Second. WILEY Blackwell, Aug. 2017 (cit. on pp. 6, 8).

[11] G. J. Tortora and B. H. Dickinson. *Principles of Anatomy and Physiology*. 12th edition. John Wiley Sons, 2008 (cit. on pp. 8, 10).

[12] Johns Hopkins Medicine. *Anatomy and Function of the Heart's Electrical System*. URL: `https://www.hopkinsmedicine.org/health/conditions-and-diseases/anatomy-and-function-of-the-hearts-electrical-system` (cit. on p. 9).

[13] S.E. Anderson, R. Lahm, and P.A. Iaizzo. *Handbook of Cardiac Anatomy, Physiology, and Devices*. Humana Press, 2009. Chap. The Coronary Vascular System and Associated Medical Devices. DOI: `https://doi.org/10.1007/978-1-60327-372-5_7` (cit. on p. 10).

[14] American Heart Association. *Understanding Blood Pressure Readings*. 2021. URL: `https://www.heart.org/en/health-topics/high-blood-pressure/understanding-blood-pressure-readings` (cit. on p. 11).

[15] WHO. *Hypertension*. URL: `https://www.who.int/news-room/fact-sheets/detail/hypertension` (cit. on p. 11).

[16] Poulter N.R., Prabhakaran D., and Caulfield M. «Hypertension». In: *Lancet* 386.9995 (2015), pp. 801–812. DOI: `doi:10.1016/s0140-6736(14)61468-9` (cit. on p. 11).

[17] Encyclopædia Britannica. *Poiseuille's equation*. 2022. URL: `https://www.britannica.com/science/Poiseuilles-equation` (cit. on p. 12).

[18] Richard E. Klabunde. *Cardiovascular Physiology Concepts*. third. Wolters Kluwer, 2021 (cit. on p. 13).

[19] N. Ranganathan, V.Sivaciyan, and F.B. Saksena. *The Art and Science of Cardiac Physical Examination*. first. Humana Press, 2007. DOI: `https://doi.org/10.1007/978-1-59745-023-2` (cit. on pp. 15–17).

[20] T. Ellis, J. McNames, and M. Aboy. «Pulse Morphology Visualization and Analysis With Applications in Cardiovascular Pressure Signals». In: *IEEE Transactions on Biomedical Engineering* 54.9 (Sept. 2007), pp. 1552–1559. DOI: `10.1109/tbme.2007.892918` (cit. on p. 15).

[21] P. Digiglio, R. Li, W. Wang, and T. Pan. «Microflotronic Arterial Tonometry for Continuous Wearable Non-InvasiveHemodynamic Monitoring». In: *Annals of Biomedical Engineering* 42.11 (June 2014), pp. 2278–2288. DOI: `10.1007/s10439-014-1037-1` (cit. on pp. 15, 17).

[22] S. Parittotokkaporn, A. Lowe, and R. Pylypchuk. «Carotid Pulse Wave Analysis: Future Direction of Hemodynamic and Cardiovascular Risk Assessment». In: *JMA Journal* 4.2 (Apr. 2021), pp. 119–128 (cit. on pp. 16–18).

[23] J. C. Dorlas and J. A. Nijboer. «Photo-ELectric Pletysmography as a monitoring device in anaesthesia». In: *British Journal of Anaesthesia* 57.5 (1985), pp. 524–530. DOI: `110.1093/bja/57.5.524` (cit. on p. 17).

[24] M. O'Rourke, C. Vlachopoulos, and W. W. Nichols. *McDonald's Blood Flow in Arteries: Theoretical, Experimental and Clinical Principles.* Humana Press, 2011 (cit. on p. 18).

[25] M. Couade. «The advent of ultrafast ultrasound in vascular imaging: a review». In: *Journal of Vascular Diagnostics* (May 2016), pp. 9–22. DOI: `http://dx.doi.org/10.2147/JVD.S68045` (cit. on p. 19).

[26] A. Plant J. Chiha, P. Mitchell, P. Kovoor, and A. Thiagalingam. «Prediction of the severity and burden of coronary artery disease using pulse wave velocity». In: *Journal of the American College of Cardiology* 65.10S (June 2015), A1665–A1665. DOI: `https://doi.org/10.1016/S0735-1097(15)61665-5` (cit. on p. 18).

[27] T. T. Van Sloten, M. T. Schram, K. van den Hurk, et al. «Local Stiffness of the Carotid and Femoral Artery Is Associated With Incident Cardiovascular Events and All-Cause Mortality». In: *Journal of the American College of Cardiology* 63.17 (2014), pp. 1739–1747. DOI: `10.1016/j.jacc.2013.12.041` (cit. on p. 18).

[28] X. R. Ding et al. «Continuous blood pressure measurement from invasive to unobtrusive». In: *IEEE Journal Biomedical and Health Informatics* 20 (2016), pp. 1455–1465 (cit. on p. 19).

[29] I. Moens. «Over de voortplantingssnelheid van den pols». PhD thesis. Leiden, 1877 (cit. on p. 19).

[30] P. Boutouyrie, M. Briet, C. Collin, S. Vermeersch, and B. Pannier. «Assessment of pulse wave velocity». In: *Artery Research* 3.1 (2009), pp. 3–8. DOI: `10.1016/j.artres.2008.11.002` (cit. on p. 20).

[31] S. Roccabianca, C. A. Figueroa, G. Tellides, and J. D. Humphrey. «Quantification of regional differences in aortic stiffness in the aging human». In: *Journal of the Mechanical Behavior of Biomedical Materials* 29.19 (2014), pp. 618–634. DOI: `https://doi.org/10.1016/j.jmbbm.2013.01.026` (cit. on p. 20).

[32] P. Boutouyrie and S.J. Vermeersch. «Determinants of pulse wave velocity in healthy people and in the presence of cardiovascular risk factors: 'establishing normal and reference values'». In: *European Society of Cardiology* 31.19 (2010), pp. 2338–2350. DOI: `10.1093/eurheartj/ehq165` (cit. on pp. 20, 21).

[33] AtCor Medical. *SphygmoCor® XCEL*. URL: `https://atcormedical.com/technology/sphygmocor/` (cit. on p. 22).

[34] DiaTecne. *PulsePen®*. URL: `https://www.pulsepen.com/pulsepen.html` (cit. on p. 22).

[35] Honeywell. *MicroForce FMA Series*. URL: `https://sps.honeywell.com/us/en/products/advanced-sensing-technologies/healthcare-sensing/force-sensors/microforce-fma-series` (cit. on pp. 23–25).

[36] ST. *STM32L452RE*. URL: `https://www.st.com/en/evaluation-tools/nucleo-l452re.html` (cit. on pp. 31, 32).

[37] ST. *Nucleo-64 board WB15CC®*. URL: `https://www.st.com/en/evaluation-tools/nucleo-wb15cc.html#st-also-like` (cit. on pp. 31, 53).

[38] Honeywell. *Digital Output for sensors-SPI communication*. URL: `https://prod-edam.honeywell.com/content/dam/honeywell-edam/sps/siot/en-us/products/sensors/force-sensors/microforce-fma-series/documents/sps-siot-force-spi-comms-tech-note-008290-ciid-156712.pdf?download=false` (cit. on pp. 33, 34).

[39] Mohammad Afaneh. *Intro to Bluetooth Low Energy*. Novel Bits, 2018 (cit. on pp. 51, 52).

[40] ST. *STM32WB15CC®*. URL: `https://www.st.com/en/microcontrollers-microprocessors/stm32wb15cc.html` (cit. on pp. 53, 54).

[41] ST. *200 mA ultra-low quiescent current LDO*. URL: `https://www.st.com/content/ccc/resource/technical/document/datasheet/group3/ed/dd/2e/c8/60/11/42/07/DM00380001/files/DM00380001.pdf/jcr:content/translations/en.DM00380001.pdf` (cit. on p. 54).

[42] Y. C. Chi, P. W. Arand, S. G. Shroff, T. Feldman, and J. D. Carroll. «Determination of pulse wave velocities with computerized algorithms». In: *American Heart Journal* 121 (1991), pp. 1460–1470 (cit. on p. 67).

[43] J. M. Bland and D. G. Altman. «Statistical methods for assessing agreement between two methods of clinical measurement». In: *International Journal of Nursing Studies* 47.8 (2010), pp. 931–936 (cit. on p. 73).